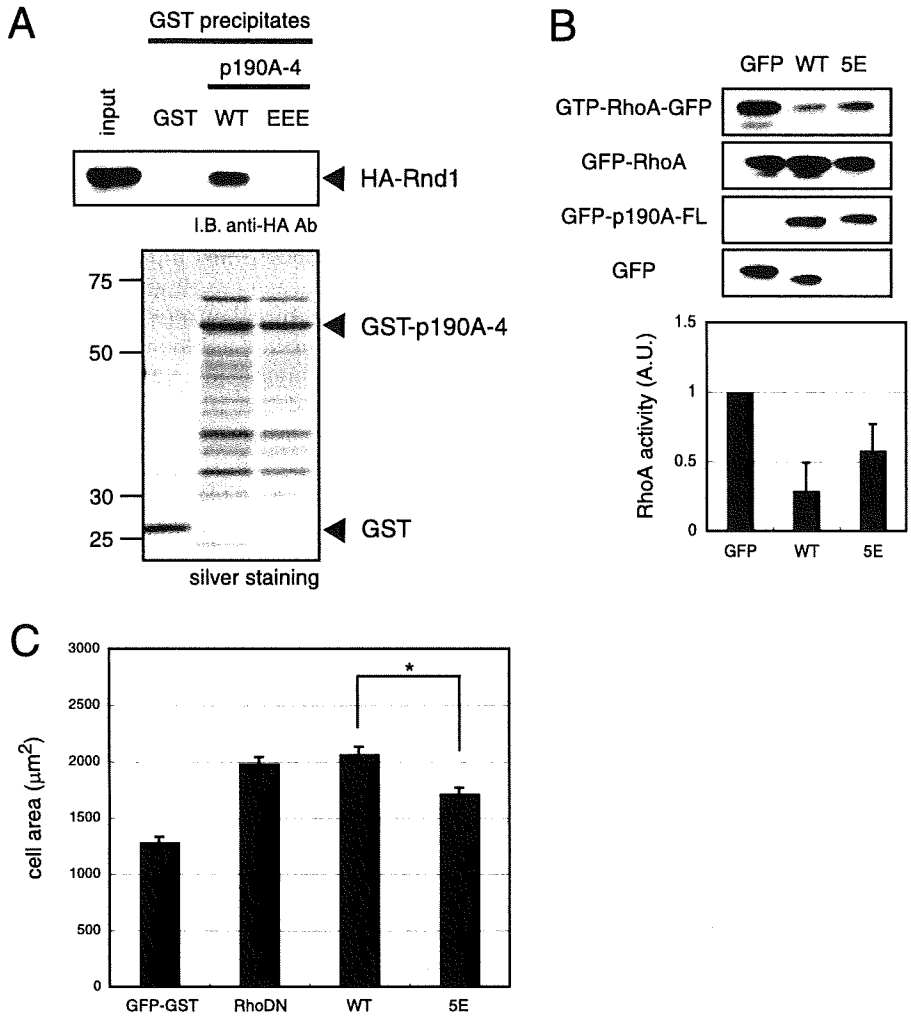

FIGURE 7. **Effects of phosphomimic mutation of p190A RhoGAP.** *A*, binding of phosphomimic mutant to Rnd1. COS7 cells were transiently transfected with pEF-BOS-HA-Rnd1. The cell lysates were incubated with glutathione-Sepharose 4B beads coated with 200 pmol of GST, GST-p190A RhoGAP-4-WT, and GST-p190A RhoGAP-4-EEE for 1 h at 4 °C. The beads were washed, and the eluates were subjected to SDS-PAGE, followed by immunoblot analysis with anti-HA Ab. GST fusion proteins were visualized by silver staining. The result is representative of three independent experiments. *B*, effect of GFP-p190A RhoGAP-FL-5E on RhoA in COS7 cells. The activity of RhoA was monitored by pulldown assay with the GST-Rhotekin-RBD. The eluates were analyzed by immunoblotting with anti-GFP Ab (*top*). The ratio of GFP-RhoA-GTP to total GFP-RhoA is shown (*bottom*). Data represent the means ± S.E. of four independent experiments. *C*, effect of phosphomimic mutant of p190A RhoGAP on vascular smooth muscle cell size. The area of cells transfected with the indicated constructs was measured. Data are indicated as mean ± S.D. ($n > 100$ in each experiment), and these results are representative of three independent experiments. The *asterisk* indicates a significant difference ($p < 0.01$) from the value of GFP-p190A RhoGAP-FL-WT.

smooth muscle (17). We found that a high concentration of ET-1 induced sustained RhoA activation (supplemental Fig. S4), whereas Y-27632 suppressed ET-1-induced sustained RhoA activation (Fig. 6*B* and supplemental Fig. S4), suggesting that Rho-kinase is involved in prolonged RhoA activation.

Because the sensitivity of the anti-p190A RhoGAP-pS1150 antibody is relatively low, we transiently transfected cultured vascular smooth muscle cells with GFP-p190A RhoGAP-FL to examine whether ET-1 induces sustained phosphorylation of p190A RhoGAP in a Rho/Rho-kinase-dependent manner (Fig. 6*C*). ET-1 induced sustained phosphorylation of GFP-p190A RhoGAP-FL at Ser^{1150}, and Y-27632 effectively inhibited ET-1-induced phosphorylation of GFP-p190A RhoGAP-FL. Under the same conditions, ET-1 induced sustained phosphorylation of MYPT1 at Thr^{853}, whereas Y-27632 completely inhibited this phosphorylation (Fig. 6*C*). Other vasoconstrictors such as angiotensin II, acetylcholine, and thrombin slightly induced phosphorylation of p190A RhoGAP (data not shown). These results suggest that ET-1 induces sustained phosphorylation of p190A RhoGAP at Ser^{1150} in a Rho/Rho-kinase-dependent manner in cultured vascular smooth muscle cells.

There are three different types of ET receptors, ET_A, ET_B, and ET_C. ET_B receptors are classified into two subtypes, ET_{B1} and ET_{B2}. ET_A and ET_{B2} receptors are expressed in vascular smooth muscle, and both receptors mediate vascular smooth muscle contraction (36). To examine which types of ET receptors are involved in phosphorylation of p190A RhoGAP, vascular smooth muscle cells transfected with GFP-p190A RhoGAP-FL were treated with a selective ET_A or ET_B antagonist. BQ-123, a selective ET_A antagonist, inhibited ET-1-induced RhoA activation and phosphorylation of p190A RhoGAP, whereas BQ-788, a selective ET_B antagonist, minimally affected ET-1-induced RhoA activation and phosphorylation of p190A RhoGAP (Fig. 6, *D* and *E*). These results suggest that ET-1 induces p190A RhoGAP phosphorylation via RhoA activation through ET_A receptor in cultured vascular smooth muscle cells.

Because the activity of p190A RhoGAP is thought to be regulated through the tyrosine phosphorylation by Src family kinases and Abl family kinases, we examined whether ET-1 affects the tyrosine phosphorylation state of p190A RhoGAP. Sodium orthovanadate, an inhibitor of phosphotyrosine phosphatase, increased the tyrosine phosphorylation level of GFP-190A RhoGAP-FL. Under the same condition, ET-1 did not induce the tyrosine phosphorylation of p190A RhoGAP (supplemental Fig. S5). These results suggest that ET-1 did not induce the tyrosine phosphorylation of p190A RhoGAP in cultured vascular smooth muscle cells.

Effect of Phosphomimic Mutant of p190A RhoGAP on Vascular Smooth Muscle Cell Size—To explore the effect of phosphorylation of p190A RhoGAP *in vitro*, we replaced three putative phosphorylation sites in p190A RhoGAP-4 with Glu to produce

GST-p190A RhoGAP-4-EEE, the phosphomimic mutants. We first examined the effect of the Glu substitution on Rnd1 binding to p190A RhoGAP. HA-Rnd1 associated with GST-p190A RhoGAP-4-WT in the pulldown assay, whereas it associated less efficiently with GST-p190A RhoGAP-4-EEE (Fig. 7*A*), suggesting that the Glu substitution weakens the binding of Rnd1 to p190A RhoGAP.

We next replaced five putative phosphorylation sites with Glu to produce GFP-p190A RhoGAP-FL-5E to examine the effect of phosphorylation of p190A RhoGAP on RhoA in intact cells. We found that the amount of GTP-bound GFP-RhoA was greater in the cells expressing GFP-p190A RhoGAP-FL-5E than that in the cells expressing GFP-p190A RhoGAP-WT, suggesting that GFP-p190A RhoGAP-5E shows a weaker GAP activity than wild type (Fig. 7*B*).

It was previously demonstrated that the constitutively active form of RhoA (RhoA Val^{14}) induces the formation of stress fibers and decreases the size of vascular smooth muscle cells through contraction, whereas the dominant negative form of RhoA (RhoA Asn^{19}) weakens the formation of stress fibers and increases the cell size (37). We employed this assay to compare the effects of p190A RhoGAP and GFP-p190A RhoGAP-FL-5E on cell contraction. The vascular smooth muscle cells were transiently transfected with GFP-RhoA Asn^{19} or GFP-p190A RhoGAP-FL-WT, and the cell sizes were measured. The expression of GFP-p190A RhoGAP-FL-WT increased the cell size under these conditions, with GFP-RhoA Asn^{19} showing increased cell size (Fig. 7*C*), suggesting that basal RhoA activity is necessary for maintaining cell contractility. GFP-p190A RhoGAP-FL-5E showed a weaker effect than that of GFP-p190A RhoGAP-FL-WT ($p < 0.01$), suggesting that the GFP-p190A RhoGAP-FL-5E mutant mimics the phosphorylation state and shows weaker activity to inactivate RhoA.

DISCUSSION

Here we show that Rho-kinase phosphorylated p190A RhoGAP in a cell-free system and identified putative phosphorylation sites, including Ser^{1150}. Rho-kinase phosphorylated p190A RhoGAP at Ser^{1150} in intact cells. Phosphorylation by Rho-kinase of the p190A RhoGAP fragment containing the GAP domain did not affect GAP activity toward RhoA in a cell-free system. However, we found that constitutively active Rho-kinase could counteract p190A RhoGAP activity in intact cells. The binding of Rnd to p190A RhoGAP is thought to enhance its GAP activity (35). Phosphorylation of p190A RhoGAP by Rho-kinase inhibited its binding to Rnd. The phosphomimic mutant of p190A RhoGAP showed the weaker Rnd binding and RhoGAP activities. Thus, it is conceivable that Rho-kinase phosphorylates p190A RhoGAP and thereby inhibits its binding to Rnd, resulting in inactivation of p190A RhoGAP and subsequent prolonged RhoA activation.

The primary action of ET-1 *in vivo* is to increase blood pressure and vascular tone. ET-1 was shown to activate Gq/G13, and to induce Ca^{2+} mobilization and subsequent phosphorylation of myosin light chain in cultured aortic smooth muscle cells (38). High concentrations of ET-1 cause long-lasting vasoconstriction (17). The transient contractile phase is mediated by G_q and Ca^{2+}/calmodulin-dependent activation of myosin light chain kinase (39). On the other hand, the sustained phase is mediated by G_{13}-dependent activation of the Rho/Rho-kinase signaling pathway (39). Consistently, high concentrations of ET-1 transiently induce Ca^{2+} mobilization in smooth muscle cells, which lasts for a minute (17).

Here we show that high concentrations of ET-1 induced sustained RhoA activation and p190RhoGAP phosphorylation in cultured vascular smooth muscle cells under the conditions in which ET-1 induced sustained MYPT1 phosphorylation. Y-27632 inhibited ET-1-induced phosphorylation of MYPT-1 as well as p190A RhoGAP and partly prohibited sustained RhoA activation, suggesting that ET-1 causes prolonged activation of the RhoA/Rho-kinase pathway. We also found that expression of p190A RhoGAP weakens the cell contractility, whereas the phosphomimic 5E mutant showed weaker activity than that of the wild type. Thus, it is possible that ET-1 induces the Rho/Rho-kinase activation and subsequent phosphorylation of p190A RhoGAP, thereby constituting the positive feedback loop to amplify Rho activation and promote contraction of vascular smooth muscle cells. ET-1 is thought to be involved in the pathogenesis of various cardiovascular diseases such as essential hypertension, pulmonary hypertension, and coronary vasospastic angina (40). The next challenge will be to explore whether p190A RhoGAP phosphorylation participates in these cardiovascular diseases.

Acknowledgments—We are grateful for Dr. T. Itoh (Nagoya City University), members of Kaibuchi Laboratory, especially Dr. T. Watanabe and Dr. T. Hikita for helpful discussion, and T. Ishii for secretarial assistance.

REFERENCES

1. Burridge, K., and Wennerberg, K. (2004) *Cell* **116,** 167–179
2. Jaffe, A. B., and Hall, A. (2005) *Annu. Rev. Cell Dev. Biol.* **21,** 247–269
3. Hartshorne, D. J., Ito, M., and Erdodi, F. (2004) *J. Biol. Chem.* **279,** 37211–37214
4. Ito, M., Nakano, T., Erdodi, F., and Hartshorne, D. J. (2004) *Mol. Cell Biochem.* **259,** 197–209
5. Matsumura, F., and Hartshorne, D. J. (2008) *Biochem. Biophys. Res. Commun.* **369,** 149–156
6. Somlyo, A. P., and Somlyo, A. V. (2003) *Physiol. Rev.* **83,** 1325–1358
7. Lemmon, M. A., and Ferguson, K. M. (2000) *Biochem. J.* **350,** 1–18
8. Rossman, K. L., Cheng, L., Mahon, G. M., Rojas, R. J., Snyder, J. T., Whitehead, I. P., and Sondek, J. (2003) *J. Biol. Chem.* **278,** 18393–18400
9. Kozasa, T., Jiang, X., Hart, M. J., Sternweis, P. M., Singer, W. D., Gilman, A. G., Bollag, G., and Sternweis, P. C. (1998) *Science* **280,** 2109–2111
10. Fukuhara, S., Murga, C., Zohar, M., Igishi, T., and Gutkind, J. S. (1999) *J. Biol. Chem.* **274,** 5868–5879
11. Suzuki, N., Nakamura, S., Mano, H., and Kozasa, T. (2003) *Proc. Natl. Acad. Sci. U. S. A.* **100,** 733–738
12. Sternweis, P. C., Carter, A. M., Chen, Z., Danesh, S. M., Hsiung, Y. F., and Singer, W. D. (2007) *Adv. Protein Chem.* **74,** 189–228
13. Bernards, A., and Settleman, J. (2004) *Trends Cell Biol.* **14,** 377–385
14. Tcherkezian, J., and Lamarche-Vane, N. (2007) *Biol. Cell* **99,** 67–86
15. Sakurada, S., Okamoto, H., Takuwa, N., Sugimoto, N., and Takuwa, Y. (2001) *Am. J. Physiol. Cell* **281,** C571–C578
16. Arthur, W. T., and Burridge, K. (2001) *Mol. Biol. Cell* **12,** 2711–2720
17. Woodsome, T. P., Polzin, A., Kitazawa, K., Eto, M., and Kitazawa, T. (2006) *J. Cell Sci.* **119,** 1769–1780
18. Loirand, G., Guerin, P., and Pacaud, P. (2006) *Circulation Res.* **98,** 322–334
19. Wettschureck, N., and Offermanns, S. (2002) *J. Mol. Med. (Berlin)* **80,** 629–638

20. Moriki, N., Ito, M., Seko, T., Kureishi, Y., Okamoto, R., Nakakuki, T., Kongo, M., Isaka, N., Kaibuchi, K., and Nakano, T. (2004) *Hypertens. Res.* **27,** 263–270
21. Kandabashi, T., Shimokawa, H., Miyata, K., Kunihiro, I., Kawano, Y., Fukata, Y., Higo, T., Egashira, K., Takahashi, S., Kaibuchi, K., and Takeshita, A. (2000) *Circulation* **101,** 1319–1323
22. Sato, M., Tani, E., Fujikawa, H., and Kaibuchi, K. (2000) *Circ. Res.* **87,** 195–200
23. Guilluy, C., Sauzeau, V., Rolli-Derkinderen, M., Guerin, P., Sagan, C., Pacaud, P., and Loirand, G. (2005) *Br. J. Pharmacol.* **146,** 1010–1018
24. Kimura, K., Fukata, Y., Matsuoka, Y., Bennett, V., Matsuura, Y., Okawa, K., Iwamatsu, A., and Kaibuchi, K. (1998) *J. Biol. Chem.* **273,** 5542–5548
25. Amano, M., Ito, M., Kimura, K., Fukata, Y., Chihara, K., Nakano, T., Matsuura, Y., and Kaibuchi, K. (1996) *J. Biol. Chem.* **271,** 20246–20249
26. Ligeti, E., and Settleman, J. (2006) *Methods Enzymol.* **406,** 104–117
27. Ren, X. D., Kiosses, W. B., and Schwartz, M. A. (1999) *EMBO J.* **18,** 578–585
28. Ridley, A. J., Self, A. J., Kasmi, F., Paterson, H. F., Hall, A., Marshall, C. J., and Ellis, C. (1993) *EMBO J.* **12,** 5151–5160
29. Settleman, J., Narasimhan, V., Foster, L. C., and Weinberg, R. A. (1992) *Cell* **69,** 539–549
30. Vincent, S., and Settleman, J. (1999) *Eur. J. Cell Biol.* **78,** 539–548
31. Mammoto, A., Huang, S., and Ingber, D. E. (2007) *J. Cell Sci.* **120,** 456–467
32. Chardin, P. (2006) *Nat. Rev. Mol. Cell. Biol.* **7,** 54–62
33. Nobes, C. D., Lauritzen, I., Mattei, M. G., Paris, S., Hall, A., and Chardin, P. (1998) *J. Biol. Chem.* **141,** 187–197
34. Harada, A., Katoh, H., and Negishi, M. (2005) *J. Biol. Chem.* **280,** 18418–18424
35. Wennerberg, K., Forget, M. A., Ellerbroek, S. M., Arthur, W. T., Burridge, K., Settleman, J., Der, C. J., and Hansen, S. H. (2003) *Curr. Biol.* **13,** 1106–1115
36. Hynynen, M. M., and Khalil, R. A. (2006) *Recent Patents Cardiovasc. Drug Discov.* **1,** 95–108
37. Worth, N. F., Campbell, G. R., Campbell, J. H., and Rolfe, B. E. (2004) *Cell Motil. Cytoskeleton* **59,** 189–200
38. Gohla, A., Schultz, G., and Offermanns, S. (2000) *Circ. Res.* **87,** 221–227
39. Hersch, E., Huang, J., Grider, J. R., and Murthy, K. S. (2004) *Am. J. Physiol.* **287,** C1209–C1218
40. Agapitov, A. V., and Haynes, W. G. (2002) *J. Renin Angiotensin Aldosterone Syst.* **3,** 1–15

Published July 13, 2009

ARTICLE

Mobile DHHC palmitoylating enzyme mediates activity-sensitive synaptic targeting of PSD-95

Jun Noritake,[1] Yuko Fukata,[1,2] Tsuyoshi Iwanaga,[1] Naoki Hosomi,[3] Ryouhei Tsutsumi,[1] Naoto Matsuda,[1] Hideki Tani,[4] Hiroko Iwanari,[3] Yasuhiro Mochizuki,[3] Tatsuhiko Kodama,[3] Yoshiharu Matsuura,[4] David S. Bredt,[5] Takao Hamakubo,[3] and Masaki Fukata[1,2]

[1]Division of Membrane Physiology, Department of Cell Physiology, National Institute for Physiological Sciences, Okazaki, Aichi 444-8787, Japan
[2]Precursory Research for Embryonic Science and Technology, Japan Science and Technology Agency, Chiyoda-ku, Tokyo 102-0075, Japan
[3]Laboratory for Systems Biology and Medicine, Research Center for Advanced Science and Technology, The University of Tokyo, Meguro-ku, Tokyo 153-8904, Japan
[4]Department of Molecular Virology, Research Institute for Microbial Diseases, Osaka University, Suita, Osaka 565-0871, Japan
[5]Department of Neuroscience, Eli Lilly and Company, Indianapolis, IN 46285

Protein palmitoylation is the most common posttranslational lipid modification; its reversibility mediates protein shuttling between intracellular compartments. A large family of DHHC (Asp-His-His-Cys) proteins has emerged as protein palmitoyl acyltransferases (PATs). However, mechanisms that regulate these PATs in a physiological context remain unknown. In this study, we efficiently monitored the dynamic palmitate cycling on synaptic scaffold PSD-95. We found that blocking synaptic activity rapidly induces PSD-95 palmitoylation and mediates synaptic clustering of PSD-95 and associated AMPA (α-amino-3-hydroxy-5-methyl-4-isoxazole propionic acid)-type glutamate receptors. A dendritically localized DHHC2 but not the Golgi-resident DHHC3 mediates this activity-sensitive palmitoylation. Upon activity blockade, DHHC2 translocates to the postsynaptic density to transduce this effect. These data demonstrate that individual DHHC members are differentially regulated and that dynamic recruitment of protein palmitoylation machinery enables compartmentalized regulation of protein trafficking in response to extracellular signals.

Introduction

Posttranslational modification, including phosphorylation, ubiquitination, and lipid modification, adds functional regulation to proteins beyond genomic information. Lipid modification increases protein hydrophobicity and plays a critical role in protein trafficking, targeting, and function. Thioester-linked palmitate modifies signaling proteins, enzymes, cytoskeletal proteins, ion channels, and scaffolding proteins and is involved in diverse aspects of cellular signaling (El-Husseini and Bredt, 2002; Resh, 2006; Linder and Deschenes, 2007). Recent global proteomic analyses have further expanded the known complement of palmitoylated proteins (Roth et al., 2006; Kang et al., 2008). Palmitoylation is unique in that it is a reversible modification and is proposed to be regulated by specific extracellular signals. Recent cell biological analyses revealed that some palmitoyl substrates such as small GTPases, Harvey Ras/neuroblastoma Ras (Rocks et al., 2005), and trimeric G proteins Gαo (Chisari et al., 2007)/Gαq (Tsutsumi et al., 2009) constitutively shuttle between the plasma membrane and the Golgi membrane by a palmitoylation/depalmitoylation cycle. This palmitate cycling generates and maintains the specific intracellular compartmentalization of substrates in nonpolarized cells (Rocks et al., 2006).

The postsynaptic scaffolding protein PSD-95 represents a major palmitoylated protein in neurons and plays critical roles in synaptogenesis and synaptic plasticity (Migaud et al., 1998; El-Husseini et al., 2000; Kennedy, 2000; Kim and Sheng, 2004; Funke et al., 2005). PSD-95 provides a platform for the postsynaptic clustering of crucial synaptic proteins, including AMPA (α-amino-3-hydroxy-5-methyl-4-isoxazole propionic

Correspondence to Masaki Fukata: mfukata@nips.ac.jp

Abbreviations used in this paper: 2-BP, 2-bromopalmitate; ABE, acyl-biotin exchange; AMPAR, AMPA receptor; βME, β-mercaptoethanol; CCD, charge-coupled device; CHX, cycloheximide; CM, chloroform-methanol; DIV, day in vitro; DN, dominant-negative; Kyn, kynurenic acid; LB, lysis buffer; miRNA, microRNA; NEM, *N*-ethyl-maleimide; NMDA, *N*-methyl-D-aspartate; PAT, palmitoyl acyltransferase; PPT, palmitoyl protein thioesterase; TARP, transmembrane AMPAR regulatory protein; TIRFM, total internal reflection fluorescence microscopy; TTX, tetrodotoxin; WT, wild type.

The Rockefeller University Press $30.00
J. Cell Biol. Vol. 186 No. 1 147–160
www.jcb.org/cgi/doi/10.1083/jcb.200903101

Supplemental Material can be found at:
http://jcb.rupress.org/cgi/content/full/jcb.200903101/DC1

Published July 13, 2009

acid) and *N*-methyl-D-aspartate (NMDA)-type glutamate receptors and cell adhesion molecules. The postsynaptic targeting of PSD-95 depends on protein palmitoylation (Topinka and Bredt, 1998). Importantly, palmitate cycling on PSD-95 is dynamically regulated by receptor activation (El-Husseini et al., 2002). Upon glutamate receptor stimulation, accelerated depalmitoylation of PSD-95 dissociates PSD-95 from postsynaptic sites and causes AMPA receptor (AMPAR) endocytosis. This receptor activation–induced depalmitoylation has also been reported in Gα (Wedegaertner and Bourne, 1994). Thus, agonist-dependent depalmitoylation down-regulates synaptic strength and G protein signaling. However, it is not yet clear whether addition of palmitate to proteins is accelerated in response to extracellular signals.

The dynamic regulation of palmitate cycling should be finely tuned by palmitoyl acyltransferases (PATs) and palmitoyl protein thioesterases (PPTs). Transmembrane proteins containing a DHHC (Asp-His-His-Cys) Cys–rich domain (DHHC proteins) have recently emerged as PATs in yeast (Bartels et al., 1999; Lobo et al., 2002; Roth et al., 2002; Linder and Deschenes, 2004). At least 23 mammalian DHHC proteins exist, and a systematic screening method has identified specific enzyme–substrate pairs (Fukata et al., 2004; Fang et al., 2006; Fernandez-Hernando et al., 2006; Fukata et al., 2006; Ponimaskin et al., 2008; Tsutsumi et al., 2009). The DHHC family is present in species ranging from yeast to human and to plants (Hemsley et al., 2005; Hemsley and Grierson, 2008). Several DHHC genes are associated with diseases, including cancers (Oyama et al., 2000), schizophrenia (Mukai et al., 2004, 2008), mental retardation (Mansouri et al., 2005; Raymond et al., 2007), and Huntington's (Yanai et al., 2006). Although the large DHHC family plays essential roles in a range of physiological functions, how the DHHC PAT family is regulated and thereby dynamically controls palmitate cycling remains uncertain.

In this study, we found that suppression of neuronal activity induces palmitoylation and synaptic accumulation of PSD-95. This activity-sensitive PSD-95 palmitoylation recruits synaptic AMPARs. Dendritically localized DHHC2 mediates this rapid synaptic palmitoylation of PSD-95. In contrast, Golgi-resident DHHC3 constitutively palmitoylates PSD-95. These experiments indicate that large DHHC family members are individually regulated, which enables their participation in specific physiological processes such as synaptic plasticity.

Results

Total internal reflection fluorescence microscopy (TIRFM) reveals the synaptic accumulation of PSD-95 upon activity blockade

To follow changes in synaptic PSD-95 accumulation over time, we first performed time-lapse imaging of cultured hippocampal neurons transfected with PSD-95–GFP by TIRFM, which excites only molecules within 100 nm of the cover glass. TIRFM preferentially visualizes wild-type (WT) PSD-95–GFP as discrete punctae on dendrites, which are not seen with cytosolic palmitoylation–deficient (CS) mutant PSD-95 or GFP (Fig. 1, A and B). We confirmed comparable expression levels of PSD-95 (WT) and PSD-95 (CS) in transfected culture (Fig. 1 B). These data confirm that palmitoylation mediates membrane trafficking and synaptic clustering of PSD-95 (Topinka and Bredt, 1998). Because PSD-95 visualized by TIRFM apposes presynaptic synaptophysin and VGLUT1 and overlaps postsynaptic NR1 NMDA receptor (Fig. 1 C), TIRFM tracks synaptic PSD-95. When ionotropic glutamate receptor activity was blocked by kynurenic acid (Kyn), the intensity of PSD-95–GFP by TIRFM steadily increased over 2 h, whereas the intensity of PSD-95 (CS) did not change (Fig. 1, D and E; and Video 1). This Kyn-induced PSD-95 increase was blocked by coapplication of 2-bromopalmitate (2-BP), which is a palmitoyl acyl transfer inhibitor. PSD-95 signals did not detectably change within 2 h of 2-BP treatment alone (Fig. 1 E). These results indicate that newly occurring palmitoylation mediates this synaptic accumulation of PSD-95. Tetrodotoxin (TTX), a blocker of action potentials, also increased PSD-95 accumulation. The dynamic change of PSD-95 intensity was specific to palmitoylation as the localizations of GFP-Rac1-CLLL (Cys-Leu-Leu-Leu), a geranylgeranylated CaaL motif, and synaptophysin-GFP, a presynaptic protein, did not change upon Kyn treatment (Fig. 1 E). Synaptic PSD-95 accumulation upon activity blockade was also confirmed by antibody staining of native PSD-95 (see Fig. 4, C and D). The effect of Kyn or TTX on PSD-95 accumulation does not reflect newly synthesized PSD-95, as cycloheximide (CHX), an inhibitor of protein synthesis, did not affect the Kyn- or TTX-induced PSD-95 increase (Fig. S1, A and B; and Video 2). Thus, PSD-95 palmitoylation increases at the postsynaptic membrane upon activity blockade. These results are complementary to receptor activation–induced depalmitoylation of PSD-95 (El-Husseini et al., 2002).

The DHHC2/15 subfamily of PSD-95 palmitoylating enzymes is regulated by synaptic activity

To monitor PSD-95 palmitoylation biochemically, we used the acyl-biotin exchange (ABE) method (Roth et al., 2006; Kang et al., 2008). We confirmed that this method specifically identified palmitoylated proteins, including PSD-95, in heterologous cells (Fig. S2 A). As previously reported (El-Husseini et al., 2002), treating neurons for 12 h with 2-BP reduced PSD-95 palmitoylation (palmitoylated PSD-95 = 13 ± 15% of control cells; $P < 0.001$; Fig. 2 A). When we treated neurons for 2 h with Kyn, the amount of palmitoylated PSD-95 significantly increased (198 ± 13% of control cells; $P < 0.001$; Fig. 2, A and B). Blocking glutamate receptors with a combination of APV (D-[-]-2-amino-5-phosphonopentanoic acid), which blocks NMDA receptors, and CNQX (6-cyano-7-nitroquinoxaline-2,3-dione), which blocks AMPARs, also enhanced PSD-95 palmitoylation within 2 h (palmitoylated PSD-95 = 184 ± 23% of control cells; $P < 0.01$). 2-BP blocked the rapid enhancement of PSD-95 palmitoylation, indicating that inhibition of depalmitoylation is not solely responsible and that newly occurring palmitoylation mediates this effect. This activity-sensitive PSD-95 palmitoylation is stoichiometric, as Kyn and APV + CNQX quantitatively

Published July 13, 2009

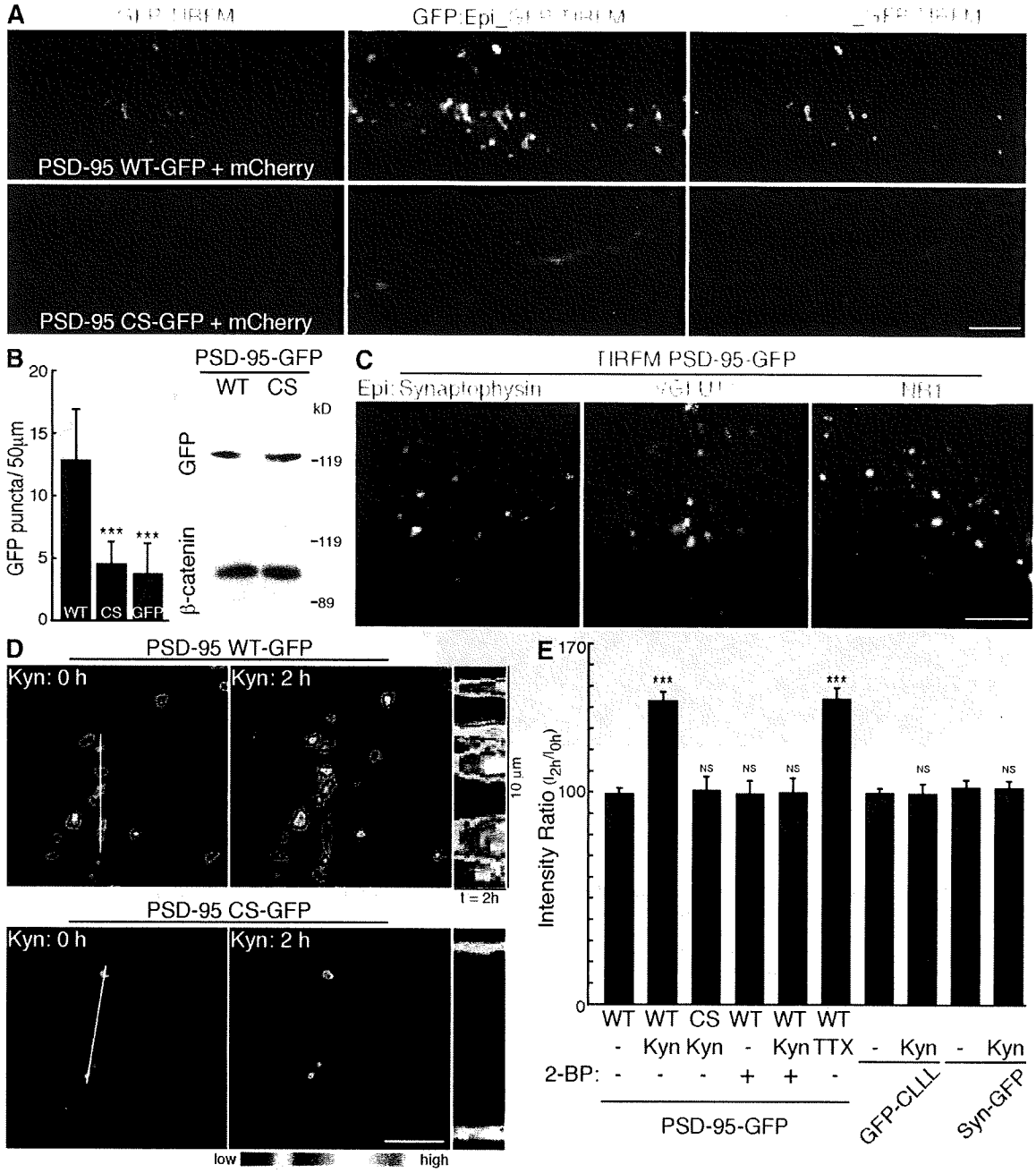

Figure 1. **TIRFM imaging of activity-sensitive PSD-95 palmitoylation.** (A) Compared with epifluorescent microscopy (Epi; green), TIRFM selectively reveals punctae from GFP-tagged PSD-95 (WT) (top; red) but not palmitoylation-deficient PSD-95 (CS) (bottom; red) in cultured hippocampal neurons. To define dendritic morphology, we coexpressed mCherry (Epi; blue). (B) TIRFM preferentially visualizes PSD-95 (WT)–GFP punctae as compared with PSD-95 (CS)–GFP or GFP alone. $n = 10$ neurons; ***, $P < 0.001$. Comparable expression levels of PSD-95 (WT)– and PSD-95 (CS)–GFP in transfected neuron culture were confirmed. (C) TIRFM tracks synaptic PSD-95. PSD-95 punctae (green) visualized by TIRFM apposed presynaptic synaptophysin and VGLUT1 and overlapped postsynaptic NR1. (D) PSD-95–GFP dynamics were analyzed by time-lapse TIRFM imaging. Inhibition of glutamate receptor activity with 10 mM Kyn increased PSD-95 (WT)–GFP intensity within 2 h. In contrast, the palmitoylation-deficient mutant PSD-95 (CS) did not change. Kymographs represent the changes in the intensity of PSD-95–GFP over 2 h. White lines indicate the regions used for the kymographs. (E) Synaptic accumulation of PSD-95 depends on newly occurring palmitoylation. Fluorescent intensities of PSD-95–GFP (WT and CS), GFP containing a C-terminal prenylation CaaL motif of Rac1 (GFP-CLLL), and synaptophysin-GFP (Syn-GFP) at 2 h after the indicated treatments were quantified. The intensity of PSD-95 (WT)–GFP but not other membrane-targeting proteins significantly increased upon 10 mM Kyn or 2 μM TTX treatment. Coapplication of 100 μM 2-BP with Kyn completely inhibited Kyn-induced increase of PSD-95–GFP intensity. $n = 3$–8 experiments; ***, $P < 0.001$ compared with control. (B and E) Error bars indicate SD. Bars: (A) 10 μm; (C and D) 5 μm.

Published July 13, 2009

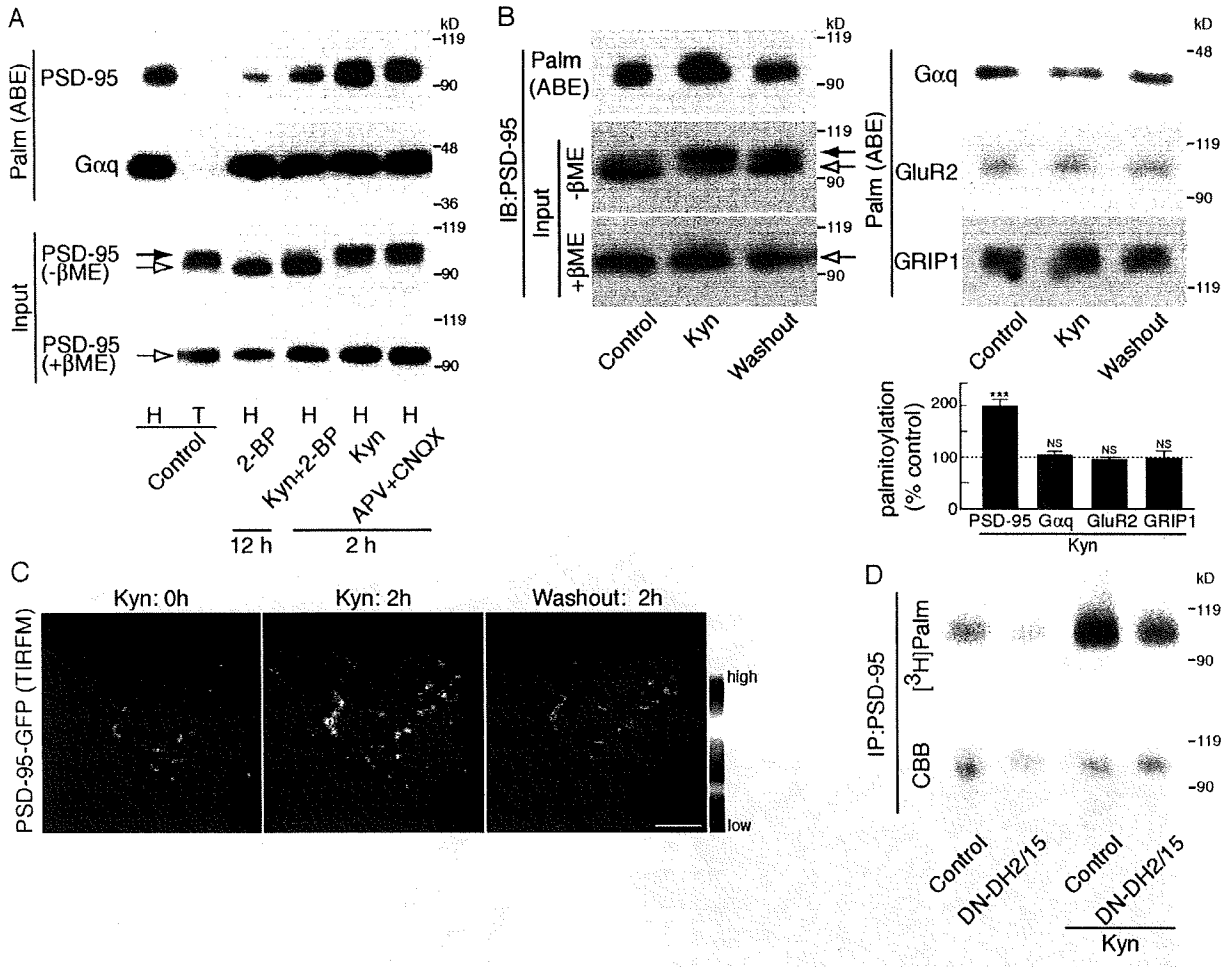

Figure 2. **The DHHC2/15 subfamily of PSD-95 PATs is regulated by synaptic activity.** (A) Activity blockade induces quantitative palmitoylation of PSD-95 but not Gαq. Hydroxylamine (H)-sensitive palmitoylated proteins were purified from treated neurons by the ABE method. The amount of palmitoylated PSD-95 and Gαq was analyzed by Western blotting. T, Tris treatment as a control of hydroxylamine. (B and C) Kyn-induced PSD-95 palmitoylation and synaptic accumulation were reversible upon washing out Kyn. (B) Treatment of hippocampal neurons with Kyn for 2 h enhanced PSD-95 palmitoylation. After washout, PSD-95 palmitoylation level returned to the basal level within 2 h (ABE), with consistent mobility change of PSD-95 (−βME). In contrast, Gαq, GluR2, and GRIP1 palmitoylation did not change upon activity blockade. Kyn-induced palmitoylation changes were quantified. $n = 3$ each; ***, $P < 0.001$. Error bars indicate SD. The dashed line (100%) indicates the normalized control level. IB, immunoblot. (A and B) Closed and open arrows indicate the positions of palmitoylated and nonpalmitoylated PSD-95, respectively. (C) The increased accumulation of PSD-95–GFP upon Kyn treatment returned to the basal level at 2 h after Kyn washout. (D) Cultured hippocampal neurons expressing a DN mutant of the DHHC2 and -15 subfamily (DN-DH2/15) were treated with 3 mCi/ml [^{3}H]palmitate for 2 h in the presence or absence of Kyn. Immunoprecipitated PSD-95 was resolved by SDS-PAGE, followed by fluorography ([^{3}H]palm) and Coomassie staining (CBB). Inhibition of glutamate receptor activity with Kyn greatly enhanced PSD-95 palmitoylation. This enhancement was decreased by DN-DH2/15. IP, immunoprecipitation. Bar, 5 μm.

shifted the PSD-95 band upward (Fig. 2, A and B; Fig. S1 C; and Fig. S2 B). This upward shift reflects palmitoylation, as β-mercaptoethanol (βME), which hydrolyses the palmitoyl thioester, leaves only the lower band (Fig. 2, A and B, bottom). Both the increased PSD-95 palmitoylation and synaptic accumulation were reversible upon washing out of Kyn, indicating that this process is activity sensitive (Fig. 2, B and C).

This activity-sensitive palmitoylation is specific for PSD-95, as Gαq, GluR2, and GRIP1 palmitoylation did not change upon activity blockade (Fig. 2, A and B). Our previous study demonstrated that PSD-95 PATs are DHHC2, -3, -7, and -15, which are phylogenetically divided into two subfamilies, DHHC3/7 and DHHC2/15 (Fukata et al., 2004). Gαq PATs are DHHC3 and -7 (Tsutsumi et al., 2009), and GluR2 PAT is DHHC3 (Fig. S2 C; Hayashi et al., 2005). These substrate selectivities allowed us to ask whether synaptic activity regulates a specific PAT subfamily (i.e., DHHC2/15). We metabolically labeled hippocampal neurons with [^{3}H]palmitic acid for 2 h in the presence or absence of Kyn. We found that Kyn-enhanced PSD-95 palmitoylation was partially blocked by a dominant-negative (DN) mutant, DN-DH2/15, which specifically inhibits the DHHC2/15 subfamily (palmitoylated PSD-95 = 61 ± 15% of Kyn-treated control cells; $P < 0.01$; Fig. 2 D; Fukata et al., 2004). The partial effect of DN-DH2/15 is probably caused by the infection efficiency of DN-DH2/15. Under our conditions, ~50% of neurons were expressing DN-DH2/15,

Published July 13, 2009

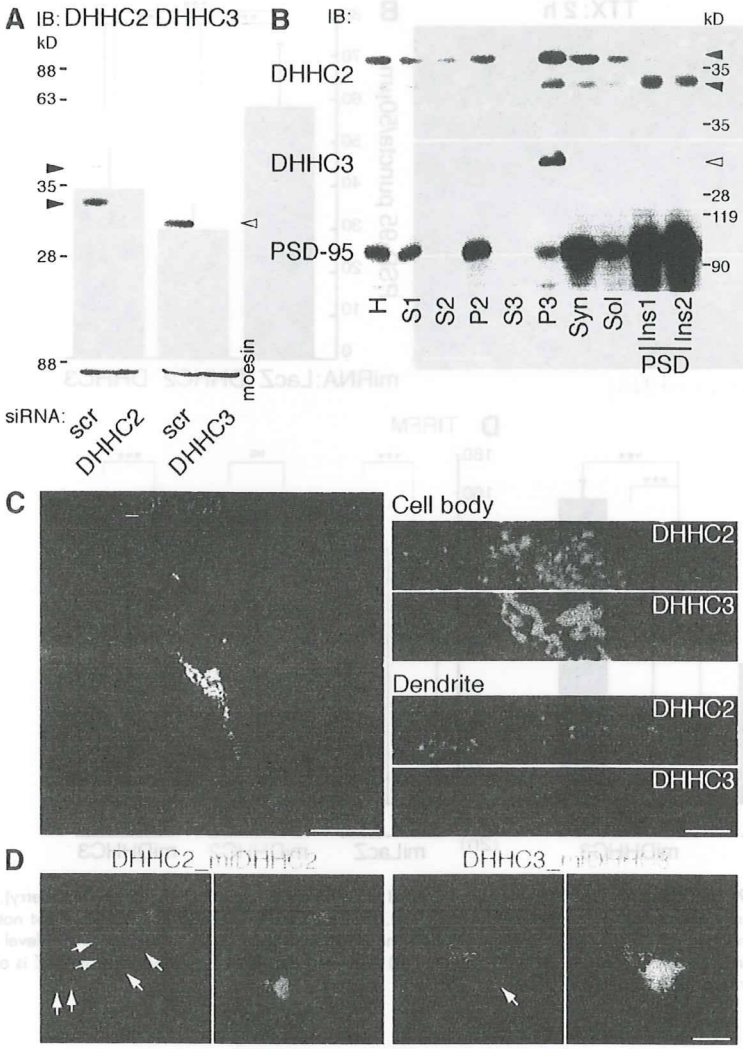

Figure 3. **Differential subcellular distribution of PSD-95 palmitoylating enzymes.** (A) Specificity of antibodies to DHHC2 and -3. The bands detected by anti-DHHC2 (closed arrowheads) and anti-DHHC3 (open arrowhead) antibodies disappeared when protein expression was knocked down by siRNAs. IB, immunoblot; scr, scramble. (B) DHHC2 was enriched in the postsynaptic density (PSD) fractions (Triton X-100–insoluble postsynaptic; closed arrowheads), whereas DHHC3 was detected in only the P3 fraction (open arrowhead). H, homogenate; S, supernatant; P, precipitate; Syn, synaptosome; Sol, Triton X-100 soluble; Ins, Triton X-100–insoluble postsynaptic density fractions. (C) DHHC2 localized in dendrites and the cell body as small vesicular structures, whereas DHHC3 specifically localized at the Golgi apparatus in 18-DIV hippocampal neurons. (D) Effective knockdown of endogenous DHHC2 and -3. Cultured hippocampal neurons were transfected with mCherry-miR RNAi (miDHHC2 and -3) expression vectors at 10 DIV. 18-DIV neurons were stained by DHHC2 or -3 antibody. Note that somatodendritic DHHC2 vesicles and Golgi DHHC3 (arrows) were not stained in mCherry-expressing knocked down neurons (red). Bars: (C [left] and D) 20 µm; (C [right]) 5 µm.

which correlates with the extent of inhibition (~40% inhibition). Although the involvement of other PATs cannot be completely ruled out, our results strongly suggest that the DHHC2/15 subfamily plays a major role in activity-sensitive PSD-95 palmitoylation.

Differential regulation of PSD-95 palmitoylating enzymes in neurons

We next examined the cellular locus for PSD-95 palmitoylation. We focused on DHHC2 and -3, as hippocampal neurons express these PATs but much less DHHC7 and -15 (Fig. S3 A). Immunoblotting with specific antibodies (Fig. 3 A) showed that DHHC2 occurred in the postsynaptic density fraction, whereas DHHC3 was present only in the P3 fraction, which contains Golgi proteins (Fig. 3 B). Consistent with this finding, DHHC3 specifically localizes to the somatic Golgi apparatus (Keller et al., 2004; Tsutsumi et al., 2009), whereas DHHC2 distributes in the dendrites and cell body as small vesicular-like structures (Fig. 3 C). These signals are specific, as the staining completely disappeared in the validated knockdown vector–transfected neuron (Fig. 3 D).

DHHC2 or -3 knockdown by microRNA (miRNA: miDHHCs) greatly reduced the number of PSD-95 punctae (Fig. 4, A and B). Importantly, knockdown of DHHC2 but not DHHC3 prevented Kyn- or TTX-induced increase of endogenous PSD-95 accumulation at synaptic sites (Fig. 4, A, C and D) and Kyn-induced augmentation of PSD-95–GFP accumulation (Fig. 5 and Video 3). The inhibitory effect of miDHHC2 was rescued by miDHHC2-resistant WT DHHC2 (WT) but not by PAT-inactive DHHC2 (CS) (Fig. 5 and Fig. S4 C). These results indicate that DHHC3 localizes to the Golgi apparatus and mediates constitutive palmitoylation of various substrates, including PSD-95, Gαq, and $GABA_A$ receptor-γ subunit (Fukata et al., 2004; Keller et al., 2004; Tsutsumi et al., 2009). In contrast, dendritic DHHC2 mediates activity-sensitive PSD-95 palmitoylation.

We next investigated whether DHHC2 PAT activity, monitored by autopalmitoylation (Fukata et al., 2004), was regulated by synaptic activity. Whereas PSD-95 palmitoylation increased

Published July 13, 2009

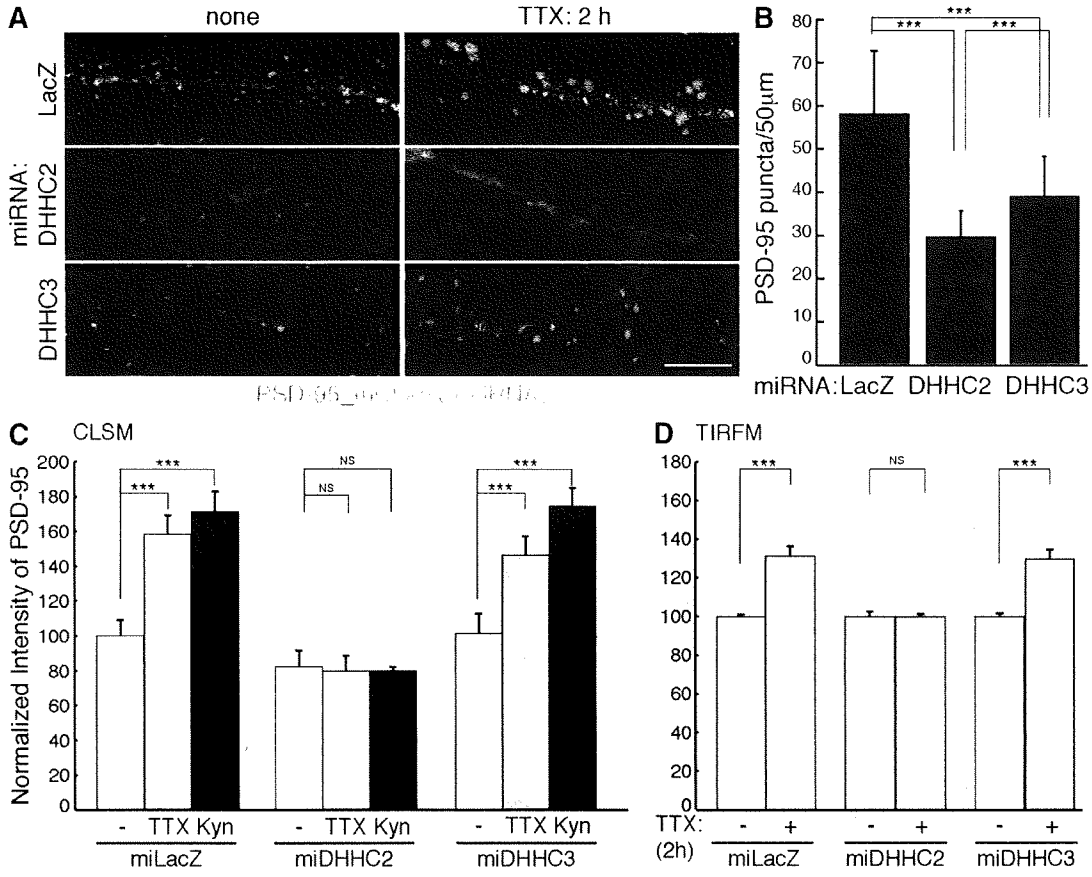

Figure 4. **DHHC2 and -3 are differently involved in PSD-95 trafficking.** (A and B) In the DHHC2 or -3 knocked down neurons (labeled with mCherry), the number of native PSD-95 puncta (green) was significantly decreased. $n = 5$ neurons; ***, $P < 0.001$. (C and D) Knockdown of DHHC2 but not DHHC3 prevented TTX- or Kyn-induced augmentation of endogenous PSD-95 accumulation. Dashed lines (100%) indicate the normalized control level. ***, $P < 0.001$. (C) Analyzed by confocal laser-scanning microscopy (CLSM). $n = 10$–15 neurons. (D) Analyzed by TIRFM. $n = 5$ neurons. miLacZ is a control miRNA targeting LacZ (β-galactosidase). (B–D) Error bars indicate SD. Bar, 5 μm.

upon TTX or Kyn treatment, autopalmitoylation of DHHC2 and -3 did not change (Fig. 6 A), suggesting that DHHC2 activity may remain constant. We then investigated whether DHHC2 localization is regulated by synaptic activity. TIRFM imaging revealed that more DHHC2 was recruited near the membrane upon Kyn or TTX treatment (Fig. 6, B and C; and Video 4), where PSD-95 localized (Fig. S4 A). This translocation was activity sensitive as it was reversible upon washing out of Kyn (Fig. 6 D). Furthermore, we found that Kyn or TTX steadily induced colocalization of endogenous DHHC2 with PSD-95 over 48 h (Fig. 6, E and F), whereas DHHC3 remained at the Golgi apparatus (Fig. S4 B).

Because PSD-95 anchors AMPARs at the postsynaptic sites through interaction with stargazin and related transmembrane AMPAR regulatory proteins (TARPs; Chen et al., 2000; Nicoll et al., 2006), we investigated changes in synaptic AMPARs upon activity blockade. We took advantage of the pHluorin-tagged GluR1 (pH-GluR1) subunit (Ashby et al., 2004; Yudowski et al., 2007) and TIRFM imaging to monitor specifically surface-expressed GluR1 (Video 5). pH-GluR1 punctate intensity was invariant over 12 h (Fig. 7, A and D; and Video 6). In contrast, TTX treatment gradually and continually increased pH-GluR1 intensity (Fig. 7, B and D; and Video 7). By post hoc immunostaining with PSD-95, we found that pH-GluR1 punctae by TIRFM completely overlapped PSD-95 clusters (Fig. 7 C). Furthermore, knockdown of DHHC2 or PSD-95 completely blocked this increase of pH-GluR1 intensity (Fig. 7, D and E). The effect of DHHC2 knockdown was rescued by miDHHC2-resistant WT DHHC2 (WT) but not by PAT-inactive DHHC2 (CS) (Fig. 7 E and Video 8). The effect of PSD-95 knockdown was rescued by short hairpin RNA–resistant WT PSD-95 (WT) but not by palmitoylation-deficient PSD-95 (CS) (Fig. 7 E, Fig. S4 D, and Video 9). We also found that knockdown of DHHC2 or PSD-95 similarly inhibited Kyn-induced increase of pH-GluR1 (Fig. 7 D). pH-GluR2, endogenous GluR1, GluR2, and stargazin-like TARPs but neither NR2A NMDA receptor nor VGLUT1 showed an increase similar to that of pH-GluR1 (Fig. S5).

Published July 13, 2009

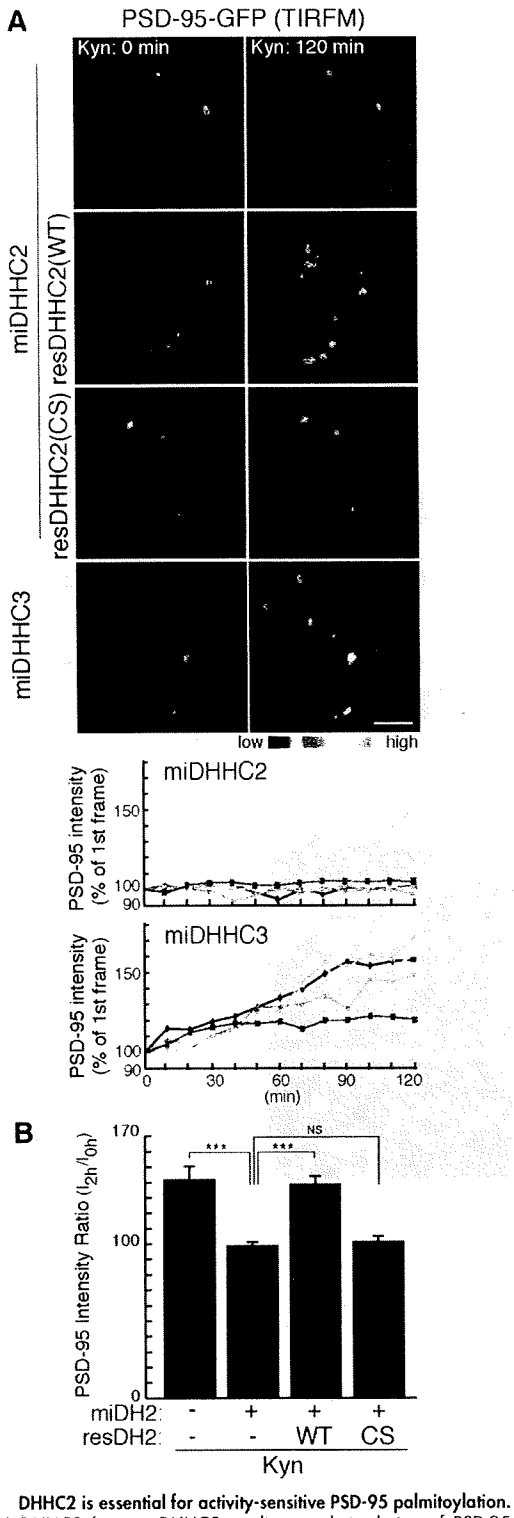

Figure 5. **DHHC2 is essential for activity-sensitive PSD-95 palmitoylation.** (A and B) DHHC2 but not DHHC3 mediates palmitoylation of PSD-95 upon activity blockade. Knockdown of DHHC2 but not DHHC3 inhibited Kyn-induced PSD-95–GFP recruitment at the synaptic membrane. miDHHC2-resistant DHHC2 (WT) but not PAT-inactive DHHC2 (CS) rescued Kyn-induced PSD-95 accumulation. (A) TIRFM intensity of representative five punctae from a neuron was plotted with time. (B) $n = 3$ each; ***, $P < 0.001$. Error bars indicate SD. Bar, 5 µm

Similar inhibitory effects of DHHC2 or PSD-95 knockdown were observed for endogenous GluR1, GluR2, and TARPs (Fig. S5 G). These results indicate that activity-sensitive PSD-95 palmitoylation by DHHC2 mediates the homeostatic increase of AMPARs.

By contrasting two representative PSD-95 palmitoylating enzymes, this study is the first to define differential regulation of DHHC-type palmitoylating enzymes. DHHC3 stably localizes at the Golgi apparatus and constitutively palmitoylates numerous substrates, including Gα, GluR2, and PSD-95. In contrast, dendritically localized DHHC2 senses changes in synaptic activity and rapidly translocates near postsynaptic membranes. Synaptically translocated DHHC2 induces rapid, specific, and stoichiometric palmitoylation and synaptic accumulation of PSD-95 and thereby AMPAR recruitment at postsynaptic sites. Thus, activity-sensitive DHHC2 translocation marks sites for AMPAR accumulation through compartmentalized PSD-95 palmitoylation. Complementing these findings, previous works showed that the *Drosophila melanogaster* DHHC17/HIP14 homologue localizes primarily to presynaptic terminals and acts on presynaptic Cys string protein and SNAP-25 (Ohyama et al., 2007; Stowers and Isacoff, 2007). The DHHC family members show distinctive subcellular distributions and different intracellular dynamics upon physiological stimuli. These distinctive properties provide mechanisms for specific control of protein palmitoylation by the large family of DHHC proteins.

Recent fluorescence recovery after photobleaching and photoconversion analyses revealed that several palmitoylated proteins such as Harvey Ras/neuroblastoma Ras (Rocks et al., 2005), Gαo (Chisari et al., 2007), and Gαq (Tsutsumi et al., 2009) rapidly shuttle between the plasma membrane and the Golgi apparatus. This constitutive shuttling comprises four steps: (1) palmitoylation by the Golgi-resident DHHC proteins, (2) trafficking to the plasma membrane, (3) depalmitoylation by a putative PPT and rapid cytosolic diffusion, and (4) transient trapping at the Golgi for repalmitoylation (Fig. 8 A; Rocks et al., 2006; Tsutsumi et al., 2009). In neurons, where the Golgi apparatus is segregated from the axon and dendrites, we suggest that Golgi-localized DHHC3 mediates the constitutive palmitoylation of PSD-95 at the cell body. In dendrites, PSD-95 depalmitoylated at the postsynaptic membrane diffuses from dendritic spine to shaft, is repalmitoylated on DHHC2-positive vesicles, and is redirected to postsynaptic membranes (Fig. 8 B). When synaptic activity is blocked, DHHC2 vesicles translocate from dendritic shafts to sites near the postsynaptic membrane. This allows DHHC2 to repalmitoylate PSD-95 in the spine (Fig. 8 C). Thus, mobile DHHC2 induces a local increase of PSD-95 palmitoylation, which leads to AMPAR recruitment. We propose that extracellular signals translocate specific DHHC PATs and create a new route for substrate shuttling between loci of palmitoylation and depalmitoylation, leading to efficient and precise substrate targeting. Such a compartmentalized regulatory mechanism of DHHC PATs may contribute to spatiotemporal

Published July 13, 2009

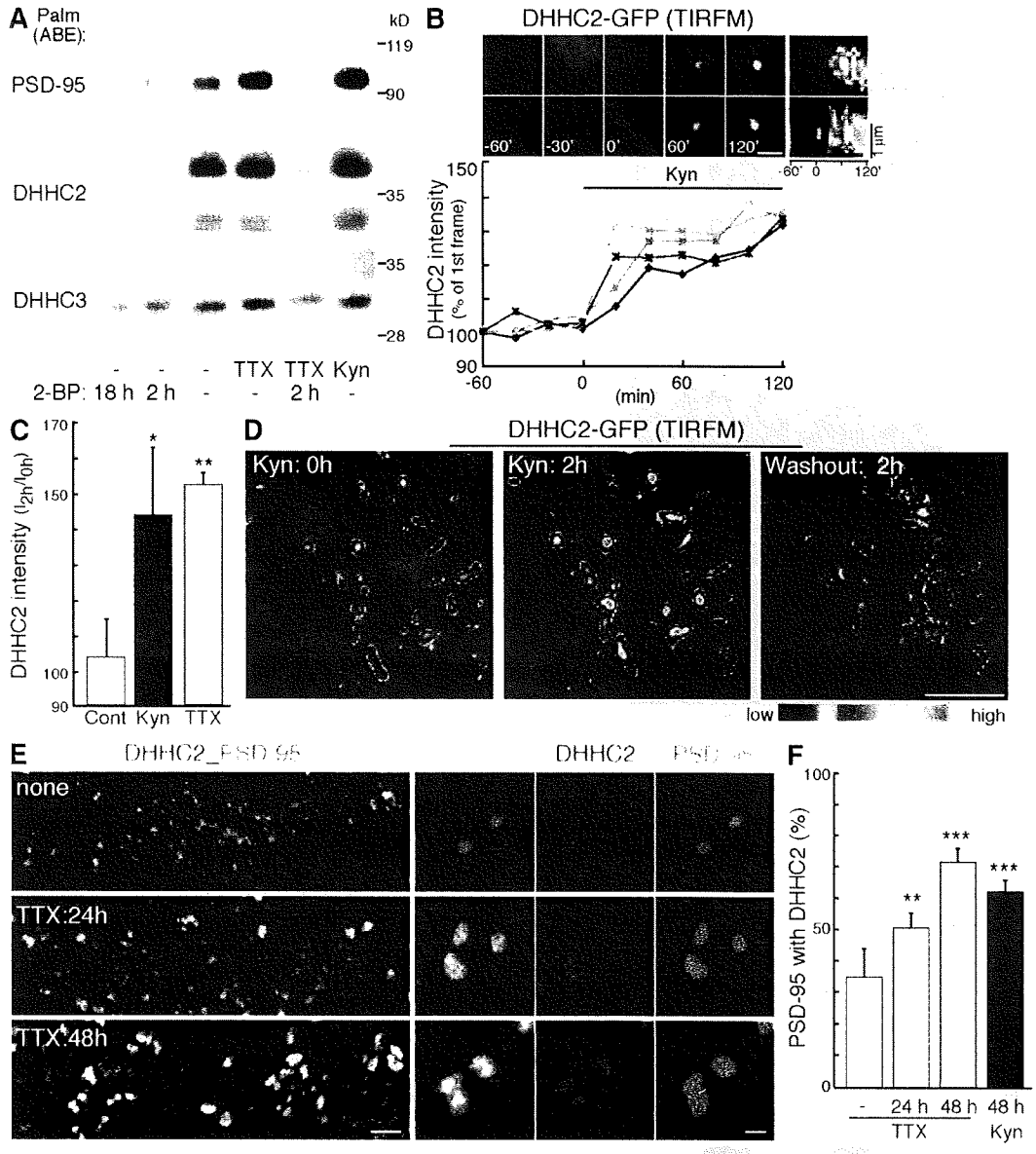

Figure 6. **Activity-sensitive synaptic translocation of DHHC2.** (A) No change in DHHC autopalmitoylation (detected by the ABE method) was seen upon activity blockade (TTX or Kyn) of hippocampal neurons, suggesting that DHHC activity remains constant. (B and C) TIRFM imaging revealed that treatment with Kyn or TTX translocated DHHC2-GFP near the plasma membrane. $n = 3$; *, $P < 0.05$; **, $P < 0.01$ compared with control. Kymographs (pseudo-color) represent the changes in the intensity of DHHC2-GFP over time. (D) The translocation of DHHC2-GFP induced by Kyn treatment was reversible upon washing out Kyn. (E and F) Colocalization of endogenous DHHC2 with PSD-95 steadily increased over prolonged TTX or Kyn treatment. (F) $n = 5$–7 each; **, $P < 0.01$; ***, $P < 0.001$. (C and F) Error bars indicate SD. Bars: (B) 2 μm; (D) 5 μm; (E [left]) 3 μm; (E [right]) 1 μm.

regulation of signaling molecules in polarized neurons, epithelial cells, and migrating cells.

This study monitors intracellular dynamics of palmitoylated proteins by taking advantage of time-lapse TIRFM, which visualizes membrane-associated proteins with exquisite sensitivity. This approach allowed us to follow dynamic changes in membrane-associated PSD-95–GFP over time in individual neurons. However, one may ask whether endogenous PSD-95 shows similar dynamics and whether TIRFM visualizes a limited set of synaptic contacts. The TIRFM limitation was supplemented with epifluorescent and confocal microscopic analyses on endogenous PSD-95. Also, our biochemical approaches, including metabolic labeling and the ABE method, showed that blocking synaptic activity quantitatively increases endogenously palmitoylated PSD-95, supporting the specificity of TIRFM imaging as a method for monitoring palmitoylated proteins in living cells.

A previous study reported that glutamate receptor activation accelerates depalmitoylation of PSD-95, dissociates PSD-95 from postsynaptic sites, and causes AMPAR endocytosis

Published July 13, 2009

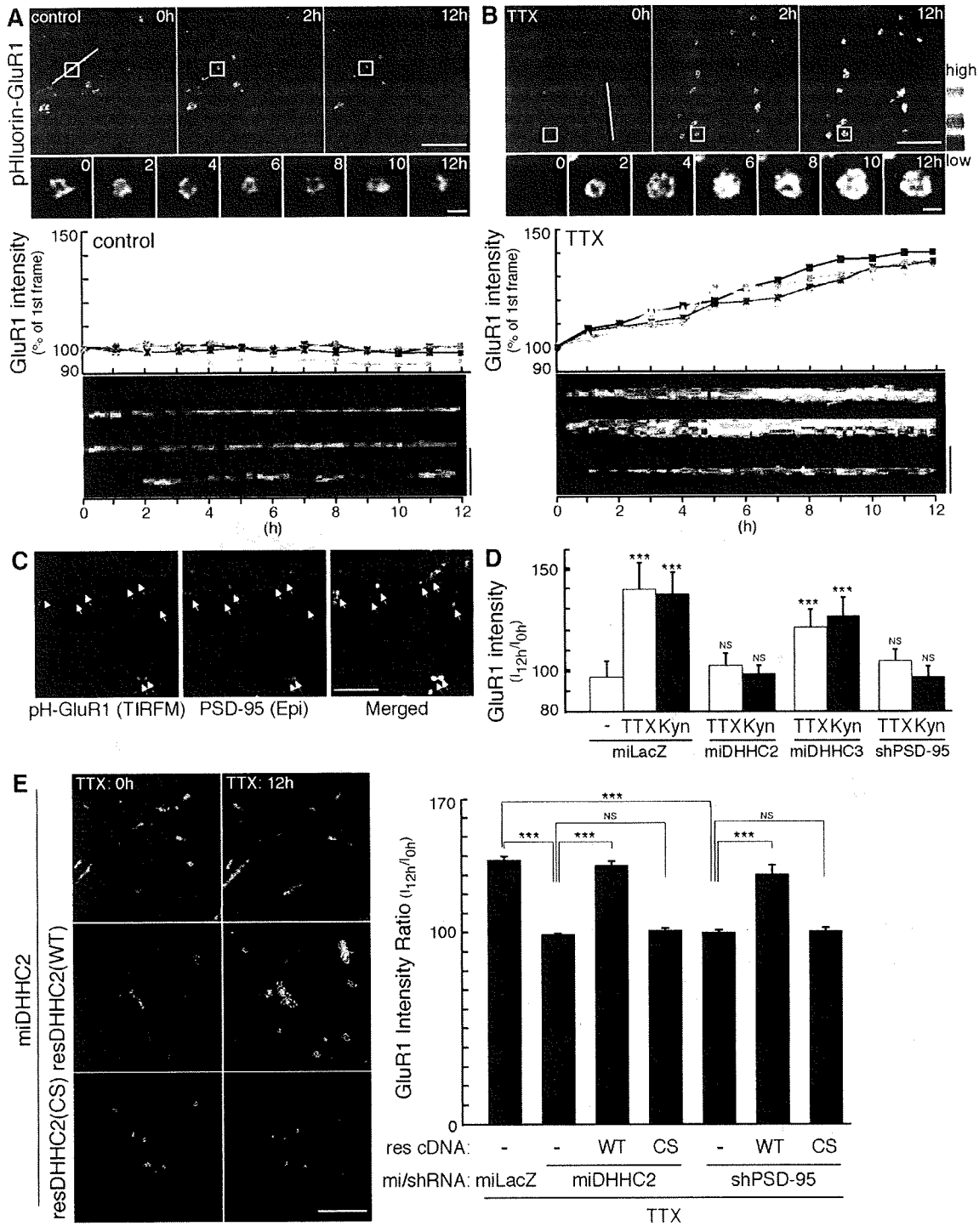

Figure 7. **Essential role of DHHC2-mediated PSD-95 palmitoylation in AMPAR homeostasis.** (A and B) Upon 2 µM TTX treatment, TIRFM intensity of pH-GluR1 punctae gradually and continually increased over a 12-h observation. Fluorescence intensity was displayed in pseudocolor and was plotted with time. Kymographs represent the changes in the intensity of pH-GluR1. White lines indicate the regions used for the kymographs. Insets are magnified in the middle panels. (C) Post hoc immunostaining with PSD-95 showed that all GluR1 punctae by TIRFM overlapped synaptic PSD-95 clusters (arrows). (D) Quantification of fluorescent intensities of pH-GluR1 by TIRFM at 12 h after TTX or Kyn treatment. Knockdown of DHHC2 or PSD-95 completely inhibited the homeostatic increase of surface GluR1. $n = 3$ each; ***, $P < 0.001$ compared with nontreated control. miLacZ is a control miRNA targeting LacZ. (E) The inhibitory effect of DHHC2 knockdown was rescued by miDHHC2-resistant DHHC2 (WT) but not by PAT-inactive DHHC2 (CS). Furthermore, the inhibitory effect of PSD-95 knockdown was rescued by short hairpin RNA–resistant PSD-95 (WT) but not by palmitoylation-deficient PSD-95 (CS). $n = 3$ for each; ***, $P < 0.001$. (D and E) Error bars indicate SD. Bars: (A and B [top] and C) 10 µm; (A and B [insets]) 0.5 µm; (A and B [bottom] and E) 5 µm.

Published July 13, 2009

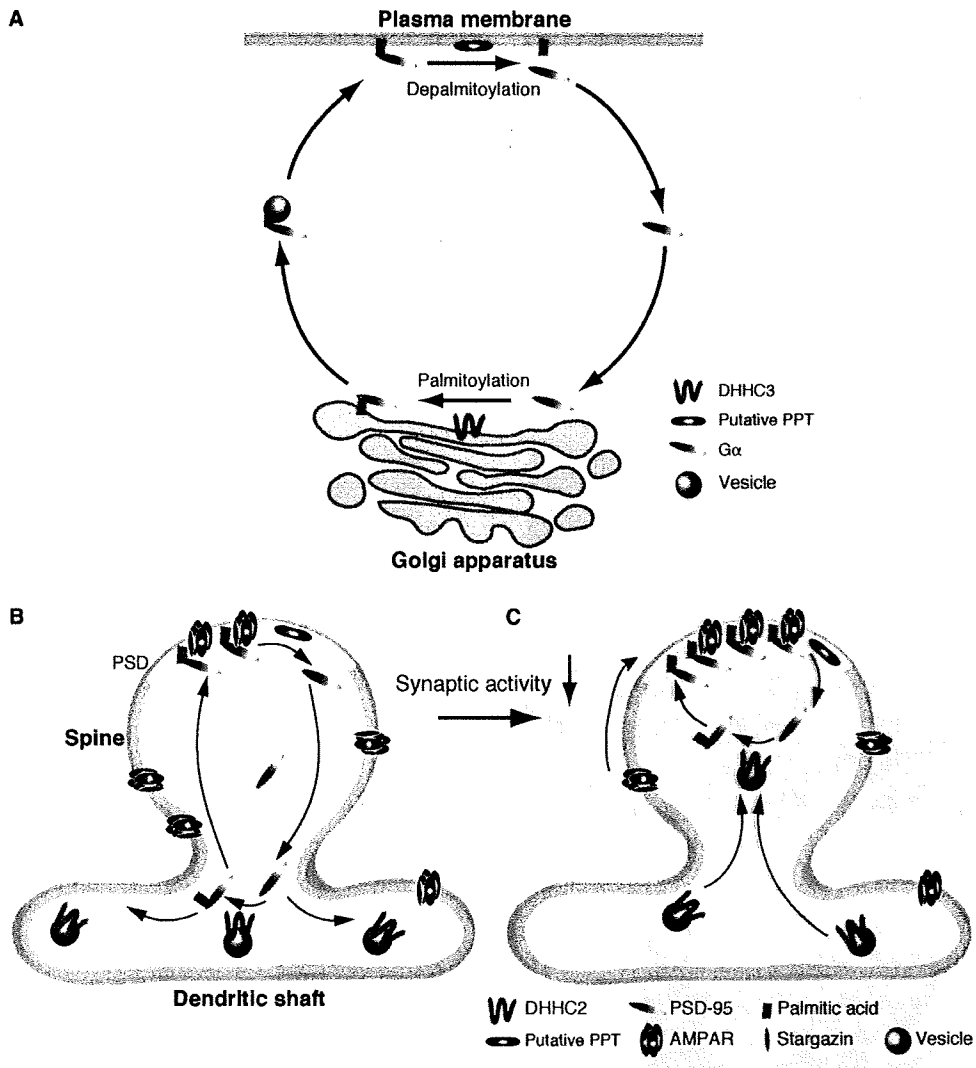

Figure 8. **Model for compartmentalized synaptic palmitoylation of PSD-95 by mobile DHHC2.** (A) Certain palmitoylated proteins such as the Gα subunit shuttle between the plasma membrane and the Golgi in nonpolarized cells. Golgi-resident DHHC3 and a putative PPT at the plasma membrane can mediate this constitutive shuttling. In neurons, DHHC3 localizes at the Golgi apparatus and mediates constitutive palmitoylation of various substrates, including Gα and PSD-95. (B and C) PSD-95 shuttling in dendrites. (B) A dynamic equilibrium exists between palmitoylated postsynaptic PSD-95 and nonpalmitoylated cytosolic PSD-95. Depalmitoylated PSD-95 diffuses into the spine and dendritic shaft. DHHC2 PAT mainly localizes in dendritic shafts on vesicles and mediates dendritic PSD-95 palmitoylation. PSD, postsynaptic density. (C) When synaptic activity is blocked, DHHC2 vesicles move into spines. This translocated DHHC2 palmitoylates spinous PSD-95; the increased postsynaptic PSD-95 thereby contributes to AMPAR homeostasis.

(El-Husseini et al., 2002). This sequence suggested that a PPT serves as the regulatory trigger. In contrast, our work demonstrates that activity blockade–induced PSD-95 palmitoylation up-regulates synaptic AMPARs. Thus, the palmitoylation/depalmitoylation cycle of PSD-95 bidirectionally contributes to AMPAR homeostasis (O'Brien et al., 1998; Turrigiano et al., 1998; Stellwagen and Malenka, 2006). By analogy, β-adrenergic receptor activation markedly accelerates depalmitoylation of Gαs, shifts Gαs to the cytoplasm, and down-regulates β-adrenergic receptor–mediated signaling (Wedegaertner and Bourne, 1994). Collectively, these studies suggest that palmitate cycling may generally mediate homeostasis of receptor-mediated signaling.

Recently, it was shown that both PSD-95 and PSD-93 play important roles in AMPAR trafficking (Elias et al., 2006). In this study, we found that knockdown of PSD-95 alone completely blocks the TTX- or Kyn-induced recruitment of AMPARs to the synapse. One may wonder why knockdown of PSD-95 alone completely blocks the TTX- or Kyn-induced AMPAR recruitment. We quantified expression levels of PSD-95 and PSD-93 in our cultured 18-d in vitro (DIV) hippocampal neurons by quantitative Western blotting. We found that PSD-95 expresses about eight times as much as PSD-93 (Fig. S3 B). Furthermore, we found that PSD-93–β, one of the major PSD-93 isoforms (Firestein et al., 2000; Parker et al., 2004), is specifically palmitoylated by the DHHC3 and -7 subfamily but not

Published July 13, 2009

by the DHHC2 and -15 subfamily (Fig. S3 C), indicating that PSD-93–β palmitoylation is differently regulated from PSD-95 palmitoylation. Furthermore, it was reported that palmitoylation of PSD-93–α and PSD-93–β is not necessary for their postsynaptic targeting (Firestein et al., 2000). Collectively, we conclude that PSD-95 plays a major role in DHHC2-mediated AMPAR recruitment upon activity blockade.

Global proteomic studies indicate that palmitoylation represents a common posttranslational modification (Roth et al., 2006; Kang et al., 2008). Importantly, many palmitoylated proteins are key signaling molecules that subserve physiological processes. Furthermore, mutations of DHHC family members have been detected in cancers (Oyama et al., 2000; Mansilla et al., 2007; Yamamoto et al., 2007) and neurological disorders (Mukai et al., 2004, 2008; Mansouri et al., 2005; Yanai et al., 2006; Raymond et al., 2007). Elucidation of molecular mechanisms for palmitoylation lays a foundation to understand its role in physiological and pathological conditions. Because DHHC enzymes show substrate specificity, DHHC PATs represent exciting therapeutic targets. Our experiments of differential partitioning and regulation on DHHC PATs should serve as a prototype for understanding how dynamic protein palmitoylation is regulated in divergent signaling environments.

Materials and methods

Materials

The following antibodies were used: rabbit polyclonal antibodies to DHHC3/GODZ (Abcam), Gαq (Santa Cruz Biotechnology, Inc.), GluR1 (EMD; Millipore), GRIP1 (Millipore), PSD-93 (Millipore), and stargazin/TARP (Millipore); a guinea pig polyclonal antibody to VGLUT1 (Millipore); and mouse monoclonal antibodies to β-catenin (BD), GluR2 (Millipore), HA (Covance), NMDAR1 (Millipore), PSD-95 (Thermo Fisher Scientific), and synaptophysin (Sigma-Aldrich). Anti–PSD-93 antibody was raised against (aa 336–379) and detected all isoforms of PSD-93. Rabbit polyclonal antibodies to GFP, PSD-95, and moesin were raised against GFP (aa 1–239), GST–PSD-95 (aa 1–434), and GST-moesin (aa 307–577), respectively, and affinity purified. A mouse monoclonal antibody to DHHC2 was raised by a baculovirus display method, which is useful for the production of antibodies against membrane proteins (Masuda et al., 2003; Saitoh et al., 2007). The following reagents were used: Kyn and APV (Tocris); TTX (Nacalai Tesque, Inc.); CNQX and CHX (Sigma-Aldrich); and 2-bromohexadecanoic acid (2-BP; Fluka).

For knockdown experiments in HEK293 cells, siRNAs from QIAGEN were used: scramble (Allstars negative control), siDHHC2, and siDHHC3. siRNA and plasmid-based miRNA for DHHCs were validated by two methods: (1) reduced expression of exogenously expressed DHHC proteins in HEK293 cells (Western blotting) and (2) down-regulation of endogenous mRNAs in HEK293 cells (quantitative real-time PCR).

Cloning and plasmid constructions

The rat cDNAs of synaptophysin (GenBank/EMBL/DDBJ accession no. NM_012664), DHHC2 (GenBank/EMBL/DDBJ accession no. AF228917), DHHC3 (GenBank/EMBL/DDBJ accession no. NM_001039014), DHHC7 (GenBank/EMBL/DDBJ accession no. NM_133394), and DHHC15 (GenBank/EMBL/DDBJ accession no. AY886531) were cloned from rat brain total RNA by RT-PCR. Synaptophysin was subcloned into pCAGGS-GFP, and DHHC2, -3, -7, and -15 were subcloned into pEF-Bos-HA and pcDNA3.1. The mutant rat DHHC2(C156S) was generated by using site-directed mutagenesis. pGW1-rat PSD-95–GFP, pGW1-rat PSD-93–β-GFP and pEF-Bos-HA-mouse DHHC constructs were described previously (El-Husseini et al., 2002; Fukata et al., 2004; Parker et al., 2004). pGW1–PSD-95–HA was constructed by replacing a GFP fragment with a synthetic DNA fragment encoding HA. pEGFP-C1-Rac1-CLLL was described previously (Nakagawa et al., 2001). To obtain the antigen for antibody production, DHHC2 was subcloned into the pcDNA-His-Flag vector. His-Flag–tagged DHHC2 was then subcloned into pAcYM1 for baculovirus production. DHHC2 was also subcloned into pGW1-GFP. To obtain Thy1/pH-GluR1, we first inserted pHluorin between residues 21 and 22 of rat GluR1 (Tomita et al., 2004) and subcloned pH-GluR1 into a Thy1 expression cassette. pCAGGS–pH-GluR2 was made by inserting pHluorin between residues 23 and 24 of mouse GluR2 (Fukata et al., 2005). cDNA of NR2A-GFP (Luo et al., 2002) was subcloned into the pCAGGS vector.

In cultured hippocampal neurons, DHHC2 and -3 were knocked down by the miR-RNAi system (Invitrogen). We used BLOCK-iT RNAi Designer (Invitrogen) to select the targeting sequences, and the following targeting sequences were used (targeting both rat and human sequences): miDHHC2, 5′-GGTGAACAATTGTGTTGGATT-3′ (alternative sequence, 5′-TGTGCATAGTGTCCATGGAAA-3′; both sequences yielded similar results); miDHHC3, 5′-TGAGACGGGAATAGAACAATT-3′; and miLacZ, 5′-GACTACACAAATCAGCGATTT-3′ (as a negative control). After subcloning these oligonucleotides into pcDNA6.2-EmGFP-miR (Invitrogen), EmGFP was replaced with mCherry, and the pre-miRNA expression cassette of pcDNA6.2-mCherry-miR (or pcDNA6.2-EmGFP-miR) was transferred to the pCAGGS vector with a β-actin promoter. PSD-95 was knocked down as described previously (Elias et al., 2006), replacing GFP of pLLox3.7 (American Type Culture Collection) with mCherry. DHHC2 (on pEF-Bos-HA-rat DHHC2) and PSD-95 (on pGW1-rat PSD-95–HA) rescue constructs that have two and four different nucleotides in the target sequences were generated by using site-directed mutagenesis (DHHC2, 5′-GGTGAACAACTGCGTTGGATT-3′; PSD-95, 5′-TCACAATAATAGCCCAGTATA-3′; changed nucleotides are underlined). All PCR products were analyzed by DNA sequencing.

pcDNAI-Gαq-GFP was provided by C.A. Berlot (Weis Center for Research, Danville, PA; Hughes et al., 2001). The cDNAs of pHluorin and mCherry were provided by J.E. Rothman (Columbia University, New York, NY; Miesenbock et al., 1998) and R.Y. Tsien (University of California, San Diego, La Jolla, CA; Shaner et al., 2005), respectively. cDNAs of rat GluR1, NR2A-GFP, and pEGFP-C1-Rac1-CLLL were gifts from R. Huganir (Johns Hopkins University, Baltimore, MD), S. Vicini (Georgetown University School of Medicine, Washington, DC), and K. Kaibuchi (Nagoya University, Showa-Ku, Nagoya, Japan), respectively. Thy1 expression cassette was provided by D. Monard (Friedrich Miescher Institute, Basel, Switzerland; Luthi et al., 1997).

Time-lapse imaging with TIRFM

Hippocampal neuron cultures were prepared from rat embryonic day 18–19 embryos. All animal experiments described herein were reviewed and approved by the ethical committee in our institutes and were performed according to the institutional guidelines concerning the care and handling of experimental animals. Neurons were seeded at a density of 2.5×10^5 cells per 3.5-cm glass-based dish (Iwaki) in neurobasal medium (Invitrogen) supplemented with B-27 supplement (Invitrogen) and 2 mM Glutamax (Invitrogen). 8–10-DIV neurons were transfected by Lipofectamine 2000 (Invitrogen) and observed (18–21 DIV) at 37°C in a microincubator (MI-IBC-IF; Olympus) with an inverted microscope (IX81; Olympus) equipped with a Plan-Apochromat 100× NA 1.45 oil TIRFM objective lens, an ImageEM charge-coupled device (CCD) camera (C9100-13; Hamamatsu Photonics) and Meta Imaging software version 7.1 (MDS Analytical Technologies). A 488-nm laser was used as a light source. Time-lapse images were taken every 10 min with a laser-based zero drift autofocusing system (IX81-ZDC; Olympus), which adjusts the focal plane to the initial focal plane just before each imaging frame. The video files (QuickTime Movie) were produced with ImageReady 2.0 (Adobe Systems, Inc.). To quantitate changes in PSD-95–GFP, DHHC2-GFP, or pH-GluR1 intensity by TIRFM, we randomly chose fields, and the punctae (>1.25 µm in diameter) were quantitated in every frame. Fluorescent intensities from TIRF images were analyzed using MetaMorph software version 7.1 (MDS Analytical Technologies). The ratios of intensities at 0–120 min (for PSD-95 and DHHC2) or 0–12 h (for GluR1) in 50–100 randomly selected punctae (three to eight independent experiments) are shown. Kymographs were produced using Meta Imaging software version 7.1.

Immunofluorescence analysis of hippocampal neuron culture

Cultured hippocampal neurons (5×10^4 cells) were seeded onto 12-mm coverslips in 24-well dishes. 18–28-DIV neurons were fixed with 4% paraformaldehyde/120 mM sucrose/100 mM Hepes, pH 7.4, at room temperature for 10 min, permeabilized with 0.1% Triton X-100 for 10 min, and blocked with PBS containing 10 mg/ml BSA for 10 min on ice. For staining of DHHC2 and VGLUT1, neurons were fixed with methanol for 10 min at −30°C. For mouse anti-DHHC2 antibody, Alexa Fluor 488–conjugated anti–mouse IgG_1 subtype specific (Invitrogen) was used as a secondary antibody. For surface GluR1 and GluR2 staining, GluR1 and GluR2 receptors were "live" labeled with an antibody to an extracellular

epitope of GluR1 (EMD) or GluR2 (Millipore) by incubating neurons in conditioned medium for 15 min at 37°C. Neurons were then fixed with 2% paraformaldehyde for 20 min and blocked as described above. Surface GluR1 and GluR2 were visualized with Alexa Fluor 488–conjugated secondary antibody. Fluorescent images were taken with a confocal laser-scanning microscopy system (LSM5 Exciter; Carl Zeiss, Inc.) equipped with a Plan-Apochromat 63× NA 1.40 oil immersion objective lens. For knockdown experiments, 8–12-DIV neurons were transfected with pCAGGS-mCherry-miR vectors by Lipofectamine 2000. At 8–10 d after transfection, neurons were stained with anti-DHHC2, DHHC3, PSD-95, GluR1, GluR2, and stargazin/TARP antibodies. To quantitate the intensity of PSD-95 clusters and surface GluR1, surface GluR2, or TARP clusters (costained with PSD-95), we randomly chose 10–15 fields from two independent neuronal cultures (on treated and age-matched sister control cultures) and analyzed the three largest caliber proximal dendrites (20 µm long; at least 400 clusters). We measured the mean intensities of individual clusters (>1 µm diameter) along these dendritic segments. Microscope control and all image analyses were performed with ZEN software (Carl Zeiss, Inc.). Brightness and contrast adjustments were applied to the whole image using Photoshop CS3 (Adobe Systems, Inc.). For some experiments, immunolabeled samples were observed by TIRFM and epifluorescent microscopy.

ABE method

The ABE method was performed as previously described (Roth et al., 2006; Kang et al., 2008) and modified for cultured neurons. After treating 18–28-DIV hippocampal neurons (5×10^5 cells/6-well dish) with the indicated antagonists or inhibitors, neurons were washed with PBS containing 10 mM *N*-ethyl-maleimide (NEM) twice and solubilized with 0.1 ml of lysis buffer (LB; 50 mM Tris-HCl, pH 7.5, 5 mM EDTA, and 50 mM NaCl) containing 2% SDS and 10 mM NEM. After 15 min of extraction, LB with 2% Triton X-100 and 10 mM NEM was added to a final volume of 1 ml and incubated for 1 h at 4°C. After centrifugation at 20,000 *g* for 10 min, the supernatants were precipitated by the chloroform-methanol (CM) method (Wessel and Flugge, 1984). Precipitated protein was solubilized in 0.2 ml SB (50 mM Tris-HCl, pH 7.5, 5 mM EDTA, and 4% SDS) containing 10 mM NEM at 37°C for 10 min. The protein was diluted into 0.8 ml LB with 0.2% Triton X-100 and 1 mM NEM and incubated overnight at 4°C. NEM was removed by three sequential CM precipitations. Precipitated protein was solubilized in 0.2 ml of buffer SB, and then 0.8 ml HB (1 M hydroxylamine, pH 7.5, 150 mM NaCl, 0.2% Triton X-100, and 1 mM biotin-HPDP) or buffer TB (1 M Tris-HCl, pH 7.5, 150 mM NaCl, 0.2% Triton X-100, and 1 mM biotin-HPDP) was added. The mixture was incubated for 1 h at room temperature and subjected to CM precipitation. The precipitated protein was dissolved in 0.2 ml SB, diluted into 0.8 ml LB containing 150 mM NaCl, 0.2% Triton X-100, and 200 µM biotin-HPDP, and incubated for 1 h at room temperature. Free biotin-HPDP was removed by CM precipitation. The precipitated protein was solubilized in 100 µl of buffer UB (50 mM Tris-HCl, pH 7.5, 5 mM EDTA, and 2% SDS) and diluted in 900 µl LB with 0.2% Triton X-100. After brief centrifugation, the supernatant was incubated with 30 µl neutravidin-agarose (Thermo Fisher Scientific) for 1 h at 4°C. After washing the beads with LB containing 0.1% SDS and 0.2% Triton X-100, bound proteins were suspended in SDS-PAGE sample buffer (62.5 mM Tris-HCl, pH 6.8, 10% glycerol, 2% SDS, and 0.001% bromophenol blue) with 10 mM DTT (without βME; −βME) and boiled at 90°C for 2 min. To see the palmitoylation-dependent mobility shift of PSD-95, the cell lysate was treated similarly (−βME). To reduce the sample completely, the lysate was separately treated with SDS-PAGE sample buffer with 2% βME at 100°C for 5 min (+βME). Samples were subjected to SDS-PAGE and Western blotting with the indicated antibodies.

In vivo palmitate labeling

Hippocampal neurons were infected with Semliki forest virus to express GFP or GFP-tagged DN DHHC2/15 (Fukata et al., 2004). At 24 h after infection, cells were labeled for 2 h in neurobasal media containing 3 mCi/ml [^{3}H]palmitic acid (PerkinElmer) either in the presence or absence of 10 mM Kyn. Labeled cells were washed with PBS and resuspended in 0.15 ml LB A (20 mM Tris-HCl, pH 7.5, 1 mM EDTA, 100 mM NaCl, and 1% SDS). After 5 min of extraction, 1% Triton X-100 was added to a final volume of 1.5 ml. After centrifugation at 20,000 *g* for 10 min, the supernatants were incubated with rabbit anti–PSD-95 antibody for 1 h and then incubated for 1 h with 30 µl protein A–Sepharose (GE Healthcare) at 4°C. Immunoprecipitates were washed three times with buffer containing 20 mM Tris-HCl, pH 7.4, 1 mM EDTA, 100 mM NaCl, and 1% Triton X-100. Immunoprecipitated PSD-95 was suspended in SDS sample buffer. For fluorography, protein samples were separated by SDS-PAGE. Gels were treated with Amplify (GE Healthcare) for 30 min, dried under vacuum, and exposed to Biomax MS (Kodak) at −80°C for 2 wk. After autoradiography, the bands were scanned and analyzed with National Institutes of Health software.

Transfected HEK293 cells were preincubated for 30 min in serum-free DME with 5 mg/ml fatty acid–free BSA (Sigma-Aldrich). Cells were then labeled with 0.25 mCi/ml [^{3}H]palmitic acid for 4 h in the preincubation medium. Cells were washed with PBS and scraped with SDS-PAGE sample buffer with 10 mM DTT. The cell lysate was resolved by SDS-PAGE, followed by fluorography (36-h exposure) and Western blotting.

In situ hybridization

In situ hybridization on 7-µm paraffin-embedded 3-wk-old rat brain sections (Genostaff) was performed by using digoxigenin-labeled RNA probes. cDNAs of mouse DHHC2 (nt 1–1,098 from initiating ATG), rat DHHC3 (nt 1–900), rat DHHC7 (nt 1–927), rat DHHC15 (nt 1–1,014), and rat PSD-95 (nt 1,212–1,444) were used for probe templates. An antidigoxigenin antibody linked to alkaline phosphatase (Dako) and NBT/BCIP (nitro blue tetrazolium chloride/5-bromo-4-chloro-3-indolyl phosphate; Dako) substrate was used to detect hybridization signals. All sections were developed for 1 h. Images were taken with a dissection microscope (SZ61; Olympus) equipped with a digital camera (DP20; Olympus) and with an upright microscope (BX51; Olympus) equipped with a UPlan SApo 20× NA 0.75 objective lens and a CCD camera (DP72; Olympus).

Quantitative Western blotting

Bands on blotted membranes were visualized with a cooled CCD camera (Light-Capture II; ATTO), and the optimal specific bands were analyzed with the CS Analyzer 3.0 software (ATTO). For calibration, immunopurified PSD-95–GFP and PSD-93–β-GFP from transfected HEK293 cells were quantitated by Coomassie brilliant staining using BSA.

Subcellular fractionation

The method was basically followed as described previously (Carlin et al., 1980). In brief, five rat adult brains were homogenized in buffer containing 320 mM sucrose and 10 mM Hepes-NaOH, pH 7.4 (containing 0.2 mM PMSF). Homogenate was centrifuged for 10 min at 1,000 *g* to remove crude nuclear fraction (P1). The supernatant (S1) was centrifuged at 9,000 *g* for 15 min to produce a pellet (P2) and supernatant (S2). The S2 was centrifuged at 100,000 *g* for 1 h to produce a pellet (P3; microsomal fraction) and supernatant (S3). The P2 fraction was resuspended in the homogenization buffer. Discontinuous sucrose gradients containing 3 ml of the resuspended P2 material and 3 ml each of 0.8, 1.0, and 1.2 M sucrose solutions in 10 mM Hepes-NaOH, pH 7.4, were run for 2 h at 58,000 *g* (SW41 rotor; Beckman Coulter). The band between 1.0 and 1.2 M sucrose was obtained as a synaptosome fraction. This synaptosome fraction was extracted with ice-cold 0.5% Triton X-100 in 0.16 M sucrose and 6 mM Tris-HCl, pH 8.1, and then centrifuged at 32,800 *g* for 20 min to divide into soluble and insoluble fractions (Ins1; PSD-1). The pellet was resuspended in 0.5% Triton X-100, 0.16 M sucrose, and 6 mM Tris-HCl, pH 8.1, and centrifuged at 200,000 *g* for 1 h to produce a pellet (Ins2; PSD-2). 50 µg of proteins of each fraction was analyzed by Western blotting.

Statistical analysis

The results are expressed as mean ± SD. Statistical comparisons between groups were performed by the Student's *t* test.

Online supplemental material

Fig. S1 shows that synaptic PSD-95 accumulation upon activity blockade does not require protein synthesis. Fig. S2 shows the specific detection of PSD-95 palmitoylation by biochemical approaches. Fig. S3 shows that DHHC2 and -3 and PSD-95 dominantly express as compared with other family proteins in the hippocampus. Fig. S4 shows that DHHC2 translocates near the postsynaptic sites upon activity blockade. Fig. S5 shows that DHHC2 and PSD-95 are necessary for homeostatic increase of GluR2 as well as GluR1. Video 1 shows PSD-95–GFP dynamics in neurons by time-lapse TIRFM imaging and shows the increased accumulation of PSD-95–GFP upon Kyn treatment. Video 2 shows that CHX treatment does not inhibit Kyn-induced PSD-95–GFP increase at the synapse. Video 3 shows that activity-sensitive trafficking of PSD-95 is regulated by DHHC2. Video 4 shows activity-sensitive trafficking of DHHC2. Video 5 shows the specificity of pH-GluR1 imaging. Video 6 shows AMPAR (pH-GluR1) dynamics by time-lapse TIRFM imaging. Video 7 shows that pH-GluR1 intensity gradually and continually increases over 12 h upon TTX treatment. Video 8 shows the

Published July 13, 2009

requirement of palmitoylating activity of DHHC2 for homeostatic increase of GluR1. Video 9 shows the requirement of PSD-95 palmitoylation for the homeostatic increase of GluR1. Online supplemental material is available at http://www.jcb.org/cgi/content/full/jcb.200903101/DC1.

We thank K. Imoto (National Institute for Physiological Sciences, Okazaki, Aichi, Japan) and M. Nishijima (National Institute of Health Sciences, Setagaya-ku,Tokyo, Japan and Japan Science and Technology Agency, Chiyoda-ku, Tokyo, Japan) for suggestions and encouragement, K. Kaibuchi for sharing reagents, F. Perez (Institut Curie, Paris, France), A.S. Kato (Eli Lilly and Company, Indianapolis, IN), and T. Watanabe (Nagoya University, Chikusa-ku, Nagoya, Japan) for valuable suggestions, and N. Takahashi for technical support.

J. Noritake and R. Tsutsumi are supported by the Japan Society for the Promotion of Science. Y. Fukata is supported by grants from the Human Frontier Science Program (HFSP; CDA0015-07) and Ministry of Education, Culture, Sports, Science and Technology (MEXT; 21680029). M. Fukata is also supported by grants from the HFSP (RGY0059-06) and MEXT (20670005, 20022043, and 20054022).

Submitted: 18 March 2009
Accepted: 11 June 2009

References

Ashby, M.C., S.A. De La Rue, G.S. Ralph, J. Uney, G.L. Collingridge, and J.M. Henley. 2004. Removal of AMPA receptors (AMPARs) from synapses is preceded by transient endocytosis of extrasynaptic AMPARs. *J. Neurosci.* 24:5172–5176.

Bartels, D.J., D.A. Mitchell, X. Dong, and R.J. Deschenes. 1999. Erf2, a novel gene product that affects the localization and palmitoylation of Ras2 in *Saccharomyces cerevisiae*. *Mol. Cell. Biol.* 19:6775–6787.

Carlin, R.K., D.J. Grab, R.S. Cohen, and P. Siekevitz. 1980. Isolation and characterization of postsynaptic densities from various brain regions: enrichment of different types of postsynaptic densities. *J. Cell Biol.* 86:831–845.

Chen, L., D.M. Chetkovich, R.S. Petralia, N.T. Sweeney, Y. Kawasaki, R.J. Wenthold, D.S. Bredt, and R.A. Nicoll. 2000. Stargazin regulates synaptic targeting of AMPA receptors by two distinct mechanisms. *Nature.* 408:936–943.

Chisari, M., D.K. Saini, V. Kalyanaraman, and N. Gautam. 2007. Shuttling of G protein subunits between the plasma membrane and intracellular membranes. *J. Biol. Chem.* 282:24092–24098.

El-Husseini, Ael-D., and D.S. Bredt. 2002. Protein palmitoylation: a regulator of neuronal development and function. *Nat. Rev. Neurosci.* 3:791–802.

El-Husseini, A.E., E. Schnell, D.M. Chetkovich, R.A. Nicoll, and D.S. Bredt. 2000. PSD-95 involvement in maturation of excitatory synapses. *Science.* 290:1364–1368.

El-Husseini, Ael-D., E. Schnell, S. Dakoji, N. Sweeney, Q. Zhou, O. Prange, C. Gauthier-Campbell, A. Aguilera-Moreno, R.A. Nicoll, and D.S. Bredt. 2002. Synaptic strength regulated by palmitate cycling on PSD-95. *Cell.* 108:849–863.

Elias, G.M., L. Funke, V. Stein, S.G. Grant, D.S. Bredt, and R.A. Nicoll. 2006. Synapse-specific and developmentally regulated targeting of AMPA receptors by a family of MAGUK scaffolding proteins. *Neuron.* 52:307–320.

Fang, C., L. Deng, C.A. Keller, M. Fukata, Y. Fukata, G. Chen, and B. Luscher. 2006. GODZ-mediated palmitoylation of GABA(A) receptors is required for normal assembly and function of GABAergic inhibitory synapses. *J. Neurosci.* 26:12758–12768.

Fernandez-Hernando, C., M. Fukata, P.N. Bernatchez, Y. Fukata, M.I. Lin, D.S. Bredt, and W.C. Sessa. 2006. Identification of Golgi-localized acyl transferases that palmitoylate and regulate endothelial nitric oxide synthase. *J. Cell Biol.* 174:369–377.

Firestein, B.L., S.E. Craven, and D.S. Bredt. 2000. Postsynaptic targeting of MAGUKs mediated by distinct N-terminal domains. *Neuroreport.* 11:3479–3484.

Fukata, M., Y. Fukata, H. Adesnik, R.A. Nicoll, and D.S. Bredt. 2004. Identification of PSD-95 palmitoylating enzymes. *Neuron.* 44:987–996.

Fukata, Y., A.V. Tzingounis, J.C. Trinidad, M. Fukata, A.L. Burlingame, R.A. Nicoll, and D.S. Bredt. 2005. Molecular constituents of neuronal AMPA receptors. *J. Cell Biol.* 169:399–404.

Fukata, Y., T. Iwanaga, and M. Fukata. 2006. Systematic screening for palmitoyl transferase activity of the DHHC protein family in mammalian cells. *Methods.* 40:177–182.

Funke, L., S. Dakoji, and D.S. Bredt. 2005. Membrane-associated guanylate kinases regulate adhesion and plasticity at cell junctions. *Annu. Rev. Biochem.* 74:219–245.

Hayashi, T., G. Rumbaugh, and R.L. Huganir. 2005. Differential regulation of AMPA receptor subunit trafficking by palmitoylation of two distinct sites. *Neuron.* 47:709–723.

Hemsley, P.A., and C.S. Grierson. 2008. Multiple roles for protein palmitoylation in plants. *Trends Plant Sci.* 13:295–302.

Hemsley, P.A., A.C. Kemp, and C.S. Grierson. 2005. The TIP GROWTH DEFECTIVE1 S-acyl transferase regulates plant cell growth in *Arabidopsis*. *Plant Cell.* 17:2554–2563.

Hughes, T.E., H. Zhang, D.E. Logothetis, and C.H. Berlot. 2001. Visualization of a functional Galpha q-green fluorescent protein fusion in living cells. Association with the plasma membrane is disrupted by mutational activation and by elimination of palmitoylation sites, but not be activation mediated by receptors or AlF4. *J. Biol. Chem.* 276:4227–4235.

Kang, R., J. Wan, P. Arstikaitis, H. Takahashi, K. Huang, A.O. Bailey, J.X. Thompson, A.F. Roth, R.C. Drisdel, R. Mastro, et al. 2008. Neural palmitoyl-proteomics reveals dynamic synaptic palmitoylation. *Nature.* 456:904–909.

Keller, C.A., X. Yuan, P. Panzanelli, M.L. Martin, M. Alldred, M. Sassoe-Pognetto, and B. Luscher. 2004. The gamma2 subunit of GABA(A) receptors is a substrate for palmitoylation by GODZ. *J. Neurosci.* 24:5881–5891.

Kennedy, M.B. 2000. Signal-processing machines at the postsynaptic density. *Science.* 290:750–754.

Kim, E., and M. Sheng. 2004. PDZ domain proteins of synapses. *Nat. Rev. Neurosci.* 5:771–781.

Linder, M.E., and R.J. Deschenes. 2004. Model organisms lead the way to protein palmitoyltransferases. *J. Cell Sci.* 117:521–526.

Linder, M.E., and R.J. Deschenes. 2007. Palmitoylation: policing protein stability and traffic. *Nat. Rev. Mol. Cell Biol.* 8:74–84.

Lobo, S., W.K. Greentree, M.E. Linder, and R.J. Deschenes. 2002. Identification of a Ras palmitoyltransferase in *Saccharomyces cerevisiae*. *J. Biol. Chem.* 277:41268–41273.

Luo, J.H., Z.Y. Fu, G. Losi, B.G. Kim, K. Prybylowski, B. Vissel, and S. Vicini. 2002. Functional expression of distinct NMDA channel subunits tagged with green fluorescent protein in hippocampal neurons in culture. *Neuropharmacology.* 42:306–318.

Luthi, A., H. Van der Putten, F.M. Botteri, I.M. Mansuy, M. Meins, U. Frey, G. Sansig, C. Portet, M. Schmutz, M. Schroder, et al. 1997. Endogenous serine protease inhibitor modulates epileptic activity and hippocampal long-term potentiation. *J. Neurosci.* 17:4688–4699.

Mansilla, F., K. Birkenkamp-Demtroder, M. Kruhoffer, F.B. Sorensen, C.L. Andersen, P. Laiho, L.A. Aaltonen, H.W. Verspaget, and T.F. Orntoft. 2007. Differential expression of DHHC9 in microsatellite stable and instable human colorectal cancer subgroups. *Br. J. Cancer.* 96:1896–1903.

Mansouri, M.R., L. Marklund, P. Gustavsson, E. Davey, B. Carlsson, C. Larsson, I. White, K.H. Gustavson, and N. Dahl. 2005. Loss of ZDHHC15 expression in a woman with a balanced translocation t(X;15)(q13.3;cen) and severe mental retardation. *Eur. J. Hum. Genet.* 13:970–977.

Masuda, K., H. Itoh, T. Sakihama, C. Akiyama, K. Takahashi, R. Fukuda, T. Yokomizo, T. Shimizu, T. Kodama, and T. Hamakubo. 2003. A combinatorial G protein-coupled receptor reconstitution system on budded baculovirus. Evidence for Galpha and Galphao coupling to a human leukotriene B4 receptor. *J. Biol. Chem.* 278:24552–24562.

Miesenbock, G., D.A. De Angelis, and J.E. Rothman. 1998. Visualizing secretion and synaptic transmission with pH-sensitive green fluorescent proteins. *Nature.* 394:192–195.

Migaud, M., P. Charlesworth, M. Dempster, L.C. Webster, A.M. Watabe, M. Makhinson, Y. He, M.F. Ramsay, R.G. Morris, J.H. Morrison, et al. 1998. Enhanced long-term potentiation and impaired learning in mice with mutant postsynaptic density-95 protein. *Nature.* 396:433–439.

Mukai, J., H. Liu, R.A. Burt, D.E. Swor, W.S. Lai, M. Karayiorgou, and J.A. Gogos. 2004. Evidence that the gene encoding ZDHHC8 contributes to the risk of schizophrenia. *Nat. Genet.* 36:725–731.

Mukai, J., A. Dhilla, L.J. Drew, K.L. Stark, L. Cao, A.B. MacDermott, M. Karayiorgou, and J.A. Gogos. 2008. Palmitoylation-dependent neurodevelopmental deficits in a mouse model of 22q11 microdeletion. *Nat. Neurosci.* 11:1302–1310.

Nakagawa, M., M. Fukata, M. Yamaga, N. Itoh, and K. Kaibuchi. 2001. Recruitment and activation of Rac1 by the formation of E-cadherin-mediated cell-cell adhesion sites. *J. Cell Sci.* 114:1829–1838.

Nicoll, R.A., S. Tomita, and D.S. Bredt. 2006. Auxiliary subunits assist AMPA-type glutamate receptors. *Science.* 311:1253–1256.

O'Brien, R.J., S. Kamboj, M.D. Ehlers, K.R. Rosen, G.D. Fischbach, and R.L. Huganir. 1998. Activity-dependent modulation of synaptic AMPA receptor accumulation. *Neuron.* 21:1067–1078.

Ohyama, T., P. Verstreken, C.V. Ly, T. Rosenmund, A. Rajan, A.C. Tien, C. Haueter, K.L. Schulze, and H.J. Bellen. 2007. Huntingtin-interacting

protein 14, a palmitoyl transferase required for exocytosis and targeting of CSP to synaptic vesicles. *J. Cell Biol.* 179:1481–1496.

Oyama, T., Y. Miyoshi, K. Koyama, H. Nakagawa, T. Yamori, T. Ito, H. Matsuda, H. Arakawa, and Y. Nakamura. 2000. Isolation of a novel gene on 8p21.3-22 whose expression is reduced significantly in human colorectal cancers with liver metastasis. *Genes Chromosomes Cancer.* 29:9–15.

Parker, M.J., S. Zhao, D.S. Bredt, J.R. Sanes, and G. Feng. 2004. PSD93 regulates synaptic stability at neuronal cholinergic synapses. *J. Neurosci.* 24:378–388.

Ponimaskin, E., G. Dityateva, M.O. Ruonala, M. Fukata, Y. Fukata, F. Kobe, F.S. Wouters, M. Delling, D.S. Bredt, M. Schachner, and A. Dityatev. 2008. Fibroblast growth factor-regulated palmitoylation of the neural cell adhesion molecule determines neuronal morphogenesis. *J. Neurosci.* 28:8897–8907.

Raymond, F.L., P.S. Tarpey, S. Edkins, C. Tofts, S. O'Meara, J. Teague, A. Butler, C. Stevens, S. Barthorpe, G. Buck, et al. 2007. Mutations in ZDHHC9, which encodes a palmitoyltransferase of NRAS and HRAS, cause X-linked mental retardation associated with a Marfanoid habitus. *Am. J. Hum. Genet.* 80:982–987.

Resh, M.D. 2006. Palmitoylation of ligands, receptors, and intracellular signaling molecules. *Sci. STKE.* doi:10.1126/stke.3592006re14.

Rocks, O., A. Peyker, M. Kahms, P.J. Verveer, C. Koerner, M. Lumbierres, J. Kuhlmann, H. Waldmann, A. Wittinghofer, and P.I. Bastiaens. 2005. An acylation cycle regulates localization and activity of palmitoylated Ras isoforms. *Science.* 307:1746–1752.

Rocks, O., A. Peyker, and P.I. Bastiaens. 2006. Spatio-temporal segregation of Ras signals: one ship, three anchors, many harbors. *Curr. Opin. Cell Biol.* 18:351–357.

Roth, A.F., Y. Feng, L. Chen, and N.G. Davis. 2002. The yeast DHHC cysteine-rich domain protein Akr1p is a palmitoyl transferase. *J. Cell Biol.* 159:23–28.

Roth, A.F., J. Wan, A.O. Bailey, B. Sun, J.A. Kuchar, W.N. Green, B.S. Phinney, J.R. Yates III, and N.G. Davis. 2006. Global analysis of protein palmitoylation in yeast. *Cell.* 125:1003–1013.

Saitoh, R., T. Ohtomo, Y. Yamada, N. Kamada, J. Nezu, N. Kimura, S. Funahashi, K. Furugaki, T. Yoshino, Y. Kawase, et al. 2007. Viral envelope protein gp64 transgenic mouse facilitates the generation of monoclonal antibodies against exogenous membrane proteins displayed on baculovirus. *J. Immunol. Methods.* 322:104–117.

Shaner, N.C., P.A. Steinbach, and R.Y. Tsien. 2005. A guide to choosing fluorescent proteins. *Nat. Methods.* 2:905–909.

Stellwagen, D., and R.C. Malenka. 2006. Synaptic scaling mediated by glial TNF-alpha. *Nature.* 440:1054–1059.

Stowers, R.S., and E.Y. Isacoff. 2007. *Drosophila* huntingtin-interacting protein 14 is a presynaptic protein required for photoreceptor synaptic transmission and expression of the palmitoylated proteins synaptosome-associated protein 25 and cysteine string protein. *J. Neurosci.* 27:12874–12883.

Tomita, S., M. Fukata, R.A. Nicoll, and D.S. Bredt. 2004. Dynamic interaction of stargazin-like TARPs with cycling AMPA receptors at synapses. *Science.* 303:1508–1511.

Topinka, J.R., and D.S. Bredt. 1998. N-terminal palmitoylation of PSD-95 regulates association with cell membranes and interaction with K+ channel, Kv1.4. *Neuron.* 20:125–134.

Tsutsumi, R., Y. Fukata, J. Noritake, T. Iwanaga, F. Perez, and M. Fukata. 2009. Identification of G protein alpha subunit-palmitoylating enzyme. *Mol. Cell. Biol.* 29:435–447.

Turrigiano, G.G., K.R. Leslie, N.S. Desai, L.C. Rutherford, and S.B. Nelson. 1998. Activity-dependent scaling of quantal amplitude in neocortical neurons. *Nature.* 391:892–896.

Wedegaertner, P.B., and H.R. Bourne. 1994. Activation and depalmitoylation of Gs alpha. *Cell.* 77:1063–1070.

Wessel, D., and U.I. Flugge. 1984. A method for the quantitative recovery of protein in dilute solution in the presence of detergents and lipids. *Anal. Biochem.* 138:141–143.

Yamamoto, Y., Y. Chochi, H. Matsuyama, S. Eguchi, S. Kawauchi, T. Furuya, A. Oga, J.J. Kang, K. Naito, and K. Sasaki. 2007. Gain of 5p15.33 is associated with progression of bladder cancer. *Oncology.* 72:132–138.

Yanai, A., K. Huang, R. Kang, R.R. Singaraja, P. Arstikaitis, L. Gan, P.C. Orban, A. Mullard, C.M. Cowan, L.A. Raymond, et al. 2006. Palmitoylation of huntingtin by HIP14 is essential for its trafficking and function. *Nat. Neurosci.* 9:824–831.

Yudowski, G.A., M.A. Puthenveedu, D. Leonoudakis, S. Panicker, K.S. Thorn, E.C. Beattie, and M. von Zastrow. 2007. Real-time imaging of discrete exocytic events mediating surface delivery of AMPA receptors. *J. Neurosci.* 27:11112–11121.

JOURNAL OF VIROLOGY, Jan. 2010, p. 303–311 Vol. 84, No. 1
0022-538X/10/$12.00 doi:10.1128/JVI.01448-09

Pathogenesis of Hepatitis C Virus Infection in *Tupaia belangeri*▽†

Yutaka Amako,[1] Kyoko Tsukiyama-Kohara,[1,2] Asao Katsume,[1,3] Yuichi Hirata,[1] Satoshi Sekiguchi,[1] Yoshimi Tobita,[1] Yukiko Hayashi,[4] Tsunekazu Hishima,[4] Nobuaki Funata,[4] Hiromichi Yonekawa,[5] and Michinori Kohara[1]*

Department of Microbiology and Cell Biology, Tokyo Metropolitan Institute of Medical Science, 2-1-6, Kamikitazawa, Setagaya-ku, Tokyo 156-0057, Japan[1]; Department of Experimental Phylaxiology, Faculty of Medical and Pharmaceutical Sciences, Kumamoto University, 1-1-1 Honjo Kumamoto City, Kumamoto 860-8556, Japan[2]; Fuji Gotemba Research Laboratory, Chugai Pharmaceutical Company, Ltd., 135, Komakado 1 Chome, Gotemba-shi, Shizuoka 412-8513, Japan[3]; Department of Pathology, Tokyo Metropolitan Komagome Hospital, 3-18-22 Honkomagome, Bunkyo-ku, Tokyo 113-8677, Japan[4]; and Laboratory of Animal Science, Tokyo Metropolitan Institute of Medical Science, 2-1-6, Kamikitazawa, Setagaya-ku, Tokyo 156-0057, Japan[5]

Received 14 July 2009/Accepted 5 October 2009

The lack of a small-animal model has hampered the analysis of hepatitis C virus (HCV) pathogenesis. The tupaia (*Tupaia belangeri*), a tree shrew, has shown susceptibility to HCV infection and has been considered a possible candidate for a small experimental model of HCV infection. However, a longitudinal analysis of HCV-infected tupaias has yet to be described. Here, we provide an analysis of HCV pathogenesis during the course of infection in tupaias over a 3-year period. The animals were inoculated with hepatitis C patient serum HCR6 or viral particles reconstituted from full-length cDNA. In either case, inoculation caused mild hepatitis and intermittent viremia during the acute phase of infection. Histological analysis of infected livers revealed that HCV caused chronic hepatitis that worsened in a time-dependent manner. Liver steatosis, cirrhotic nodules, and accompanying tumorigenesis were also detected. To examine whether infectious virus particles were produced in tupaia livers, naive animals were inoculated with sera from HCV-infected tupaias, which had been confirmed positive for HCV RNA. As a result, the recipient animals also displayed mild hepatitis and intermittent viremia. Quasispecies were also observed in the NS5A region, signaling phylogenic lineage from the original inoculating sequence. Taken together, these data suggest that the tupaia is a practical animal model for experimental studies of HCV infection.

Hepatitis C virus (HCV) is a small enveloped virus that causes chronic hepatitis worldwide (32). HCV belongs to the genus *Hepacivirus* of the family *Flaviviridae*. Its genome comprises 9.6 kb of single-stranded RNA of positive polarity flanked by highly conserved untranslated regions at both the 5′ and 3′ ends (4, 27, 29). The 5′ untranslated region harbors an internal ribosomal entry site (29) that initiates translation of a single open reading frame encoding a large polyprotein comprising about 3,010 amino acids (35). The encoded polyprotein is co- and posttranslationally processed into 10 individual viral proteins (15).

In most cases of human infection, HCV is highly potent and establishes lifelong persistent infection, which progressively leads to chronic hepatitis, liver steatosis, cirrhosis, and hepatocellular carcinoma (9, 16, 21). The most effective therapy for treatment of HCV infection is administration of pegylated interferon combined with ribavirin. However, the combination therapy is an arduous regimen for patients; furthermore, HCV genotype 1b does not respond efficiently (19). The prevailing scientific opinion is that a more viable option than interferon treatment is needed.

The chimpanzee is the only validated animal model for in vivo studies of HCV infection, and it is capable of reproducing most aspects of human infection (5, 18, 23, 28, 35, 36). The chimpanzee is also the only validated animal for testing the authenticity and infectivity of cloned viral sequences (8, 14, 35, 36). However, chimpanzees are relatively rare and expensive experimental subjects. Cross-species transmission from infected chimpanzees to other nonhuman primates has been tested but has proven unsuccessful for all species evaluated (1).

The tupaia (*Tupaia belangeri*), a tree shrew, is a small nonprimate mammal indigenous to certain areas of Southeast Asia (6). It is susceptible to infection with a wide range of human-pathogenic viruses, including hepatitis B viruses (13, 20, 31), and appears to be permissive for HCV infection (33, 34). In an initial report, approximately one-third of inoculated animals exhibited acute, transient infection, although none developed the high-titer sustained viremia characteristic of infection in humans and chimpanzees (33). The short duration of follow-up precluded any observation of liver pathology. In addition to the putative in vivo model, cultured primary hepatocytes from tupaias can be infected with HCV, leading to de novo synthesis of HCV RNA (37). These reports strongly support tupaias as a valid model for experimental studies of HCV infection. However, longitudinal analyses evaluating the clinical development and pathology of HCV-infected tupaias have yet to be exam-

* Corresponding author. Mailing address: Department of Microbiology and Cell Biology, The Tokyo Metropolitan Institute of Medical Science, 2-1-6, Kamikitazawa, Setagaya-ku, Tokyo 156-0057, Japan. Phone: 81-3-5316-3232. Fax: 81-3-5316-3137. E-mail: kohara-mc@igakuken.or.jp.

† Supplemental material for this article may be found at http://jvi.asm.org/.

▽ Published ahead of print on 21 October 2009.

TABLE 1. Experimental HCV infections performed in this study

Tupaia no.	Inoculum		Biopsy/sacrifice[b]
	Type	Quantity (GE/tupaia)[a]	
Group I[c]			
Tup.4	RCV	1×10^7	84, 94/144 wk p.i.
Tup.5	HCR6	6×10^5	95, 105/155 wk p.i.
Tup.6	HCR6	6×10^5	95, 105/155 wk p.i.
Tup.8	RCV	1×10^7	84, 94/144 wk p.i.
Group II[d]			
Tup.9	Tup.5 (5 wk p.i.)	1×10^2	NT
Tup.10	Tup.5 (5 wk p.i.)	1×10^2	NT
Tup.11	Tup.8 (10 wk p.i.)	1×10^2	NT
Tup.12	Tup.8 (10 wk p.i.)	1×10^2	NT
Tup.13	Tup.4 (8 wk p.i.)	1×10^2	NT
Tup.14	Tup.4 (8 wk p.i.)	1×10^2	NT
Group III[e]			
Tup.15	None		92/100 wk
Tup.17	None		92/100 wk
Tup.38	None		242 wk
Tup.39	None		242 wk

[a] Viral RNA GE/tupaia was estimated by Quantitative real-time RT-PCR (GE, genome equivalents; sensitivity > 10 GE/ml serum).
[b] Liver biopsy was performed at indicated time-point. p.i., postinoculation; NT, not tested.
[c] Group I, primary infection experiment in which 1-year-old animals were inoculated with two different types of inocula.
[d] Group II, reinfection experiment, where HCV RNA-positive sera from Group I experimental infections were passaged to naive animals.
[e] GroupIII, no-infection control.

ined. In the present study, we describe the clinical development and pathology of HCV-infected tupaias over an approximately 3-year time course.

MATERIALS AND METHODS

Animals. Table 1 summarizes the tupaias used in this study. Tupaias born in laboratory captivity were obtained from the Laboratory Animal Center at the Kunming Institute of Zoology (Chinese Academy of Sciences). Tupaias were imported with permission from the Convention on International Trade in Endangered Species of Wild Fauna and Flora (7), quarantined for medical inspection, and housed individually in standard rat cages supplied with filtered air. The animals were fed a daily regimen of eggs, fruit, and the CMS-1 commercial diet for marmosets (CLEA, Japan). Their appetites and feces were carefully monitored. Animal care and experimental handling conformed to study guidelines established by the Subcommittee on Laboratory Animal Care at the Tokyo Metropolitan Institute of Science.

Patient serum used for animal infection. HCV genotype 1b serum, designated HCR6, was obtained from a patient with chronic active hepatitis C. The infectious titer of HCR6 was determined in chimpanzee and Molt4 cells and denoted plasma K (HCR6) by Shimizu et al. (24). The HCR6 serum exhibited a PCR titer of 6×10^6 genome equivalents/ml and an infectious titer of 3.7×10^4 50% chimpanzee infectious doses/ml. Serum aliquots were frozen at −80°C until they were used.

Virion reconstitution of cloned HCV. As described previously, pHCR6 (genotype 1b; 9,611 nucleotides; GenBank accession no. AY045720) is a plasmid carrying HCV genomic cDNA cloned from HCR6 serum (30). pHCR6Rz was designed for precisely trimmed RNA expression, with the entire genomic region of pHCR6Rz recloned under the control of the T7 promoter and the 5′ and 3′ distal ends flanked by hammerhead- and hepatitis D virus ribozyme-encoding sequences, respectively (22, 25).

For molecular reconstitution of HCV particles, pHCR6Rz was transfected into IMY-N9 cells as described previously (12). Briefly, semiconfluent IMY-N9 cells in 100-mm plastic dishes were transfected with 15 μg of plasmid using 40 μl of cationic lipids (DMRIE-C reagent; Life Technology) in accordance with the manufacturer's instructions. Five hours after transfection, the cells were infected with AdexCAT7 (2) (kindly provided by Y. Matsuura) at a multiplicity of infection of 20. After infection, the culture medium was replaced with Hepato-STIM (Becton Dickinson). The culture supernatants were collected at 24 h postinfection and stored at −80°C.

Virus inoculation and collection of serum samples. Animals were infected at 6 months of age. The anesthetic agent, ketamine hydrochloride, was administered intramuscularly at 50 mg/kg body weight prior to virus inoculation and bleeding of the tupaias. The inocula were introduced intravenously at 6×10^5 genome equivalents/animal for patient serum HCR6 and 1×10^7 genome equivalents/animal for reconstituted virions derived from the pHCR6Rz inoculation. Blood samples were drawn from infected and control animals pre- and postinfection. Briefly, the animals were bled weekly for 20 weeks and biweekly thereafter. At each time point, 0.5 ml of blood was drawn from the thigh vein; the sera were separated, aliquoted, and stored for subsequent assays.

Reinfection experiments were performed by transmission of HCV RNA-positive serum from group I (Table 1) to naive animals.

Serum alanine aminotransferase (ALT) concentrations were determined using a Transnase Nissui kit (Nissui Pharmaceutical Co.), standardized, and displayed as IU/liter.

RNA isolation and quantitative RTD-PCR assay for HCV RNA. Serum samples (100 μl) were tested for circulating HCV RNA in vivo using quantitative real-time detection (RTD)-PCR (TaqMan). RNA was extracted from the sera and livers of sacrificed animals using the acid guanidium-phenol chloroform method with tRNA as a carrier (3). Two tupaias (Tup.5 and Tup.6) were inoculated with patient serum HCR6. Another two animals (Tup.4 and Tup.8) were inoculated with reconstituted viral particles (RCV). Tup.15 served as a mock-infected control. Liver specimens (3- to 4-mm^2 blocks) from these tupaias were homogenized with 1.5 ml of 5 M guanidine thiocyanate using a polytron-type homogenizer (Ultra-Turrax T25; IKA Laborteehnik, Staufen, Germany). RNA was then reextracted with 4 M guanidine thiocyanate.

RNA samples were subjected to RTD-PCR on an ABI 7700 sequence detector (Applied Biosystems) as described previously (26). The extracted RNA was dissolved in 200 μl of diethyl pyrocarbonate-treated water containing 10 mM dithiothreitol and 200 units/ml RNase inhibitor in a siliconized tube. RTD-PCR was performed using 1 μg of total RNA, one set of PCR primers, and a probe for a location within the 5′ noncoding region using the EZ *rTth* RNA PCR kit (Perkin Elmer) and the ABI Prism 7700 sequence detector system. A standard curve was constructed using a 10-fold dilution series of in vitro-transcribed and previously titrated synthetic HCV RNA.

Consequently, the quantities represented by genome equivalents correspond to an absolute standard curve (26). All quantitative RTD-PCR assays were performed using duplicate samples, with both negative control serum and HCV-positive serum included. The control sera were diluted before use and were estimated to contain low copy numbers of HCV RNA (100 genome equivalents/ml serum). Samples were deemed positive for HCV RNA if both duplicates yielded PCR-amplified product. Averages of the two estimated values are shown in the figures.

Histological analysis. Tissue samples were carefully collected from anesthetized animals by abdominal incision, fixed in 10% neutral buffered formalin, embedded in paraffin, sectioned, and stained with hematoxylin and eosin (H&E). Silver and Sudan IV (Wako Pure Chemical Industries, Ltd.) staining were also carried out to visualize fiber generation and lipid degeneration, respectively. All histological staining was performed in accordance with conventional procedures. The histological status was determined using the modified hepatitis activity index scoring system, which grades necrosis and inflammation on a scale of 0 to 18 (periportal inflammation and necrosis, 0 to 10; lobular inflammation and necrosis, 0 to 4; portal inflammation, 0 to 4) (11). Fibrosis was scored using the Ishak fibrosis scale of 0 to 6 (0, no fibrosis; 1 or 2, portal fibrosis; 3 or 4, bridging fibrosis; and 5 or 6, cirrhosis). The values in each group (Table 2) represent the averages of the scores in five visual fields.

Statistical analysis. The statistical significance of differences between controls and HCV-infected animals was analyzed with the nonparametric Mann-Whitney U test. All comparisons were two tailed. The statistical analysis was conducted with SPSS 12.0 software (SPSS Inc., Chicago, IL).

RESULTS

Inoculation of HCV causes acute hepatitis and transient viremia in tupaias. To begin this study, two distinct but related inocula were chosen for infection of tupaias. Serum from a chronic hepatitis patient (designated HCR6) was chosen for its

TABLE 2. Grading: necroinflammatory scores and fibrosis

Group	Inoculum	Tupaia no.	Grade				Total	Avg	SD	Staging
			A	B	C	D				
94 wk p.i. (biopsy)										
I	HCR 6	Tup.5	0	0	0	0	0	1.3	1.5	0
		Tup.6	1	0	1	0	2			0
	RCV	Tup.4	0	0	0	0	0			0
		Tup.8	0	0	0	3	3			6
	Control	Tup.15	0	0	0	0	0	0	0	0
III		Tup.17	0	0	0	0	0			0
		Tup.38								
		Tup.39								
144 wk p.i. (sacrifice)										
I	HCR 6	Tup.5	1	0	2	3	6	5.5	3.7	0
		Tup.6	3	0	4	3	10			1
	RCV	Tup.4	0	0	0	1	1			0
		Tup.8	1	0	1	3	5			6
	Control	Tup.15						0	0	
III		Tup.17								
		Tup.38	0	0	0	0	0			0
		Tup.39	0	0	0	0	0			0

defined genotype (genotype 1b), and genetic heterogeneity was ascertained by the process of cloning consensus cDNA. The infectivity of this serum was also experimentally defined in chimpanzees; a 50% chimpanzee infectious dose was estimated at 3.7×10^4 50% chimpanzee infectious doses/ml. Furthermore, the consensus genomic sequence of HCV was cloned from the serum (pHCR6; 9,611 bases; GenBank AY045702.1). For the second inoculum (referred to as RCV), clonal viral particles were reconstituted as described in Materials and Methods. This inoculum was expected to be free of neutralizing antibodies and thus was considered potentially more infectious than patient sera. In the case of RCV infection, genetic diversification of viral RNA, also known as quasispecies, can be regarded as a direct indication of de novo synthesis of progenitor virus in vivo.

Either patient serum or cDNA-derived RCV was inoculated into tupaias (Table 1, group I). Two animals (one female and one male) were tested against each inoculum. Age-matched animals were bred as infection-free controls.

All experimental infections are described in Materials and Methods and Table 1. Prior to experimental infection, the normal serum ALT level in tupaias was measured at 22.3 IU/liter ($n = 23$).

Inoculation with patient serum HCR6 caused rapid fluctuations in the serum ALT concentrations, from two- to fivefold, in both inoculated tupaias, suggesting acute hepatitis in vivo (Fig. 1A and B). Correlative quantitative RTD-PCR revealed HCV viremia soon after serum inoculation in Tup.5, which continued to show transient viremia long term. The appearance of viremia sometimes coincided with a steep elevation in the serum ALT (Fig. 1A). Conversely, HCV RNA was not detected in the serum of Tup.6 up to 60 weeks postinoculation and only twice thereafter. Acute-phase ALT elevations (3 to 4 weeks postinoculation) in Tup.6 might represent tight control of HCV infection by the host immune system (Fig. 1B).

Distinct results were obtained for the two animals (Tup.4 and Tup.8) inoculated with RCV. Both animals displayed sustained viremia up to 10 weeks postinoculation (Fig. 1C and D), indicating persistent HCV infection and inability to eradicate the virus. Viremia was detected intermittently throughout the course of infection, sometimes accompanying the elevation of serum ALT. Humoral immune responses in Tup.5 and Tup.6 (see Fig. S1A in the supplemental material) and Tup.4 and Tup.6 (see Fig. S1B in the supplemental material) were indicated.

We performed RTD-PCR to confirm whether HCV could replicate in the tupaias' livers (Tup.4, Tup.5, Tup.6, and Tup.8) and obtained the following results (Fig. 1E): 310 ± 117 copies/μg total RNA in Tup.5, 80 ± 11 copies/μg in Tup.6, 199 ± 77 copies/μg in Tup.4, and 292 ± 48 copies/μg in Tup.8. In contrast, HCV RNA was not detected in the liver of the mock-infected animal (Tup.15).

HCV RNA was also not detected in samples from either preinoculation or age-matched, infection-free control tupaias (Table 1, group III), nor were significant elevations in serum ALT observed for any of the three infection-free controls (data not shown).

HCV causes chronic hepatitis in tupaia liver, leading to fibrosis and cirrhosis. Serum ALT and circulating HCV RNA levels in primary infected tupaias (Table 1, group I) were monitored for 3 years postinoculation. As described above, the magnitudes of serum ALT fluctuations varied substantially among infected animals (Fig. 1A, B, C, and D). Tupaia livers were examined for histological lesions in order to elucidate if HCV caused chronic hepatitis. Liver biopsies via abdominal incisions were performed at 2 years postinoculation. All animals were sacrificed at 3 years postinoculation (4.5 years for uninfected animals). H&E staining of liver specimens from HCV-infected tupaias showed infiltrating lymphocytes within sinusoids and around portal areas, indicating chronic hepatitis in the tupaia livers (Fig. 2B, D, and H). Infiltrating lymphocytes were also observed in limiting plates, indicating ongoing inflammation (Fig. 2G and H). Furthermore, a comparison of liver samples at 2 and 3 years postinoculation revealed that the